STRUCTURAL ANALYSIS OF METAL CLUSTERS USING EXAFS

A THESIS SUBMITTED TO

THE UNIVERSITY OF KENT AT CANTERBURY

IN THE SUBJECT OF CHEMICAL PHYSICS

FOR THE DEGREE

OF MASTER OF SCIENCE.

By

Paul Damien Cluskey

September 1992

Acknowledgements

My thanks go to all of the members (and honorary members) of the Neutron and X-ray scattering team (you know who you are!), who made my brief stay here all the more memorable: Jane for being totally and amazingly wonderful; Daran for laughing at my jokes (and my trousers), and Theresa for being one filament short of an ion gun. My biggest thanks must go to my supervisor, Bob Newport, who kept my infinitives from being constantly split, and my interest in physics alive throughout my time at Kent.

I should also mention some of my friends outside the group who have kept me sane(?) during my past four years at UKC, many of whom are now scattered throughout the country, particularly the Scotland Guys - John (best buddy), Nigel (worst joke-teller), Richard (for putting me in *his* acknowledgements!) and Martin (worst card-player!) for giving me the best holiday of my life; Sinead, George, Martin T, Naomi, Ian, and the rest of the Cavers, for giving me something to do on Thursday evenings; Sima for being a friend; Darren (a.k.a. 'Dazza') for giving me humour, beer and kebabs; Steve and Jackie for company during the long summer (not to mention videos!) and Mike for surviving Herne Bay with me.

Thanks also to Robert Benfield for his help with the chemistry and Daniel for his clarity of thought with the EXAFS theory.

I acknowledge receipt of funding from the University of Kent at Canterbury.

Abstract

Three gold phosphine clusters, $Au_{55}(PPh_3)_{12}Cl_6$, $Au_{55}PPh_2(C_6H_4SO_3Na)_{12}Cl_6$ and $Au_{11}\{PPh_2(p\text{-}ClC_6H_4)\}_7I_3$ (which we shall denote Au_{55}, Au^*_{55} and Au_{11} for convenience), and the large Palladium cluster approximated to $Pd_{561}phen_{36}O_{200}$ (denoted Pd_{561} here) have been studied using EXAFS.

For the gold clusters, ligand shells have been successfully modelled, and values for Au–P, Au–I and Au–Cl distances compare favourably to chemically similar compounds. Average near-neighbour bond lengths are contracted from the bulk by approximately 0.13Å (±0.004Å) for Au_{55} and 0.22Å (±0.01Å) for Au_{11}. Debye-Waller factors for samples at room temperature and at 80K are compared for Au_{55}. Results indicate clearly that static structural disorder predominates over thermally induced vibrational disorder.

Results for the large palladium cluster were limited to metal atoms only. Bond distances show that, within the limits of experimental error, no contraction/dilation occurs. Values for near neighbour distances suggest a close packed structure. Debye-Waller factors indicate a remarkably rigid structure.

Analysis is pursued further by use of the Reverse Monte-Carlo (RMC) modelling method, which gives a three dimensional particle configuration of the system consistent with the EXAFS data. Results indicate that this modelling method has distinct weaknesses when attempting to simulate this type of system.

Contents

List of Tables

List of Figures

Chapter 1

Introduction

There has been a recent upsurge in research into the chemistry and physics of small metallic clusters, both bare and those stabilized by organic ligands such as phosphine ($P(C_6H_5)_3$), the halogens (Cl, Br, I, etc.), and many other functional groups. The origins of this interest lie with the properties the clusters possess as a result of their size and bonding nature; small clusters possess little of the characteristics of bulk metals, whereas the larger clusters begin to form the electronic band structures found in colloidal systems [1]. Small bare clusters are often difficult to characterize due to their disperse nature; it is difficult to fix the size of a bare metal cluster when synthesis involves large quantities of reagents. For this reason, clusters surrounded by a ligand shell are studied, as the synthesis of compounds with a ligand shell endows the cluster with a particularly fixed stoichiometry and narrow size distribution. This

enables more meaningful experiments to be performed on the systems, with more accuracy than with a polydisperse sample. Much of the work currently with clusters, particularly those involving transition metals is devoted to the study of catalysis. Catalysts are divided into two main categories according to their physical state: Heterogeneous catalysts exist in a different physical phase to that of the surrounding reaction mixture in which they work, frequently on supports such as silica (SiO_2) or alumina (Al_2O_3) particles [2, 3, 4, 5]. Homogeneous catalysts usually work in the same physical phase as the reacting chemicals, invariably in solution.

Large metal clusters[6] are a relatively new development in transition metal chemistry, as it is only recently that preparative techniques have been able to synthesis materials containing several tens of atoms in a fixed structure and stoichiometry. The realisation that gold forms some of the most diverse cluster compounds in this field of research has led scientists to synthesise a wide range of cluster compounds of varying nuclearity and structure[7], including those cluster compounds studied here, namely: $Au_{11}\{PPh_2(p\text{-}ClC_6H_4)\}_7I_3$, $Au_{55}(PPh_3)_{12}Cl_6$, the water soluble $Au_{55}PPh_2(C_6H_4SO_3Na)_{12}Cl_6$. In addition, a giant palladium cluster approximated as $Pd_{561}phen_{36}O_{200}$ is looked at, as it also presents an interesting system in which to study, due to its interesting catalytic properties[8, 9].

Naturally, any work which can aide in the understanding of these interesting, and possibly very useful compounds, is worthwhile. With this in mind, these metal cluster

compounds (the 55-atom clusters having been synthesised quite recently) have been prepared and their local atomic environment probed with the atom-specific EXAFS (Extended X-ray Absorption Fine Structure) technique. The study of disperse metal cluster compounds using this technique is becoming more common, due to the advantageous nature of the technique - that of chemical specificity coupled with the wide range of systems that can be studied (polycrystalline, amorphous, solutions, dilute samples, even gaseous compounds), and much work has appeared over the last decade e.g. [10, 11, 12, 13, 14, 15].

EXAFS has several advantages over existing methods of structure determination such as X-ray diffraction. Firstly, the local environment of different atoms can be examined by selecting different X-ray edges to look at, and as several edges can be examined in one experiment this offers the possibility of studying the dynamics of a chemical reaction containing several different atomic species. This chemical specificity has a further advantage when looking at a sample containing small amounts of various atomic types, as with the clusters under scrutiny here. Secondly, X-ray diffraction techniques become less sensitive for smaller discrete systems, and incorrect conclusions can be drawn from results if, for instance, Miller indices relative to an FCC structure are assumed when icosahedral geometry exists[16].

1.0.1 Gold-55 cluster

Work on this sample, one of the so called 'Schmid' Clusters after the person responsible for their synthesis[17], has involved a wide array of techniques in an attempt to understand the behaviour of the cluster, on both a microscopic level using Mössbauer [18, 19], EXAFS [20, 21], and secondary ion mass spectrometry [22], and at a macroscopic level using UV spectroscopy [1, 21, 23], DC conductivity [24] and impedance measurements [25].

Most of the gold phosphine clusters are prepared in a similar fashion, namely the reduction of Ph_3PAuCl with B_2H_6, usually carried out in an organic solvent such as benzene: The purpose of the diborane in the preparation is to initially reduce the gold(I) in the initial stages of the reaction, and also to remove excess PPh_3. The original structure for Au_{55}, proposed by Schmid, is that of a close-packed core of gold atoms in a cuboctahedral arrangement, surrounded by the ligands PPh_3 - phosphine (where Ph is a phenyl ring, C_6H_5) and chlorine. This form of the cluster is shown in Figure 1.1, with the core shown as a geometric solid, with each P atom being bonded to a gold atom on the vertex of the cuboctahedron and the chlorine atoms bonded to the centres of each square face on the core. The arrangement of the phosphine ligands gives sufficient room between them for a large atom such as Cl to gain access to the square face. The choice of ligands is clearly important here, as a cluster composed of smaller atoms would need smaller ligands to avoid them overlapping.

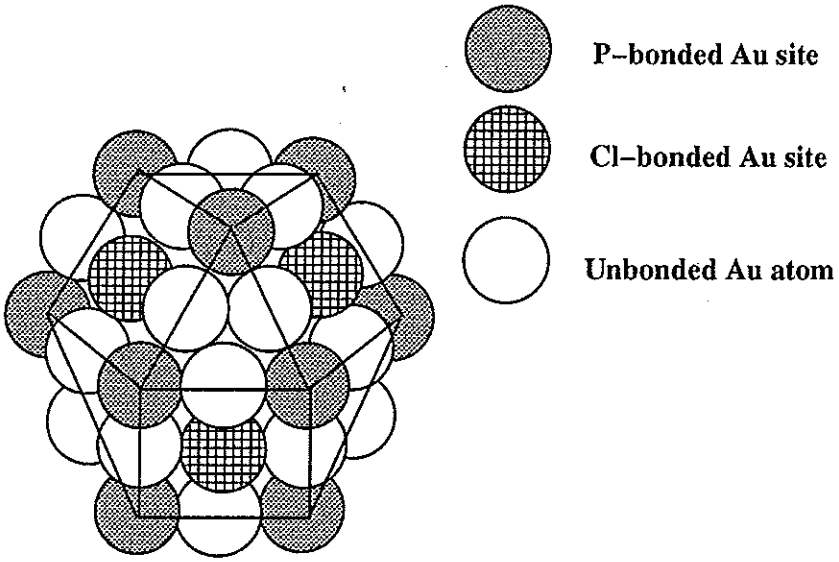

Figure 1.1: Geometric model of Au_{55} cluster, showing 'phosphine spheres'

Much evidence for the structure of this molecule exists:

(a) Mössbauer Spectroscopy.

Work performed on the cluster[18, 19] showed that four distinct sites were present in the metal core. This result validates the cuboctahedral description of the cluster, as four different types of gold atom can be said to be present, namely:

1. 13 gold atoms at the centre of the cluster, each coordinated twelvefold by near neighbours, having a similar bonding nature to that of bulk gold.
2. 24 uncoordinated surface gold atoms.
3. 6 surface Cl bonded gold atoms.
4. 12 surface P bonded gold atoms.

(b) EXAFS studies.

Previous work on the cluster using EXAFS[20, 21] has confirmed the close packed nature of the core, by comparing near neighbour distances to that of a bulk sample. The near neighbour distances for a close packed (FCC or HCP) lattice should correspond to a_0, $\sqrt{2}a_0$, $\sqrt{3}a_0$, etc (where a_0 is the nearest neighbour distance). Unfortunately little of this work has, thus far, been able to reveal any information regarding the ligand bonding to the metal core, although Marcus[21] has assigned a bond distance of 2.31Å to the Au-Cl shell.

Similar clusters containing more reactive metals (Rh) have been observed[6], and have been found to contain 20 Cl atoms per cluster due to their greater reactivity. The chlorine atoms in these clusters ($Rh_{55}[P(ter\text{-}Bu)_3]_{12}Cl_{20}$) now bond to the centre of each triangular face, and doubly to each square face.

1.0.2 Gold-11 cluster

The smaller of the two gold phosphine studied here, initially characterized by McPartlin *et al.*[26] is less of a novelty, partly due to the fact that its structure is already fairly well known; several clusters of this formation - namely $Au_{11}L_7X_3$, have been characterized using X-ray diffraction studies by Bellon and Albano[27]. Infra-Red (IR) spectroscopy and molecular weight determinations by Cariati[28] have also aided in the elucidation of the structure and stoichiometry of this compound. The cluster is

one of a series of small gold clusters, containing between 6 and 13 gold atoms, although as it does not possess the 'magic number' of atoms required for a regular stable closed shell geometry, where the nth layer consists of $(10n^2+2)$ atoms (This arises from purely geometrical considerations[29]), the structure has a somewhat distorted nature, generally considered to be an icosahedron with one of the faces replaced by a single atom, although it can also be percieved as having a modified 'chair' structure. The structure as determined from X-ray diffraction measurements is shown in Figure 1.2.

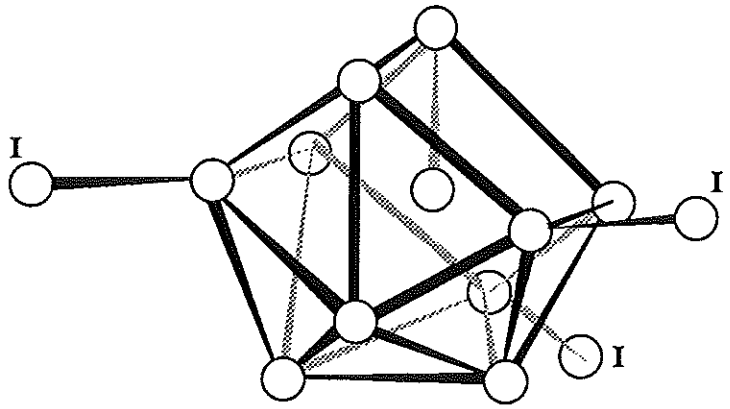

Figure 1.2: Au_{11} structure, omitting phosphine groups for clarity

As this cluster has a geometry close to that of a 13 atom icosahedron (with three of the surface atoms forming a triangle in the icosahedron replaced by a single atom), it is expected that there will be a split first neighbour bond distance evident. This arises from the fact that if hard spheres are forced into an icosahedral geometry, then the central cavity will be smaller than that required by a sphere of the same diameter.

The surface dilation was initially thought to be due to the non-bonding nature of the surface atoms in clusters of this type, giving rise to a radial bonding nature. This led to clusters of this type being referred to as 'porcupine clusters'[30] - bonding was from the central atom leading radially outwards forming 'quills', however this approach led to theoretical difficulties, and has since been superceded[7]

1.0.3 Palladium-561 Giant cluster

The formulation of this cluster as $Pd_{561}(phen)_{36}O_{200}$ is much more of an idealised nuclearity than that of the gold clusters. The close packed nature of the core (FCC) was discussed by Schmid [17] and the mean core diameter found to be 24.3Å (in the [111] direction) from X-ray measurements.

Preparation involves reduction of palladium acetate by hydrogen, in the presence of small amounts of phenanthroline (phen), followed by oxygenation with air[17]. A schematic diagram indicating the bonding of the phen groups around the core is shown in Figure 1.3, with only six of the bidentate phen ligands shown, for clarity.

Some direct experimental structural studies have been done on compounds of this type, e.g. STM (Scanning Tunneling Microscopy) imaging work by Wierenga et. al.[31], but problems exist with regards to resolving single clusters. Also, estimates of the size of the cluster were dubious using this method. Work on a similar giant cluster

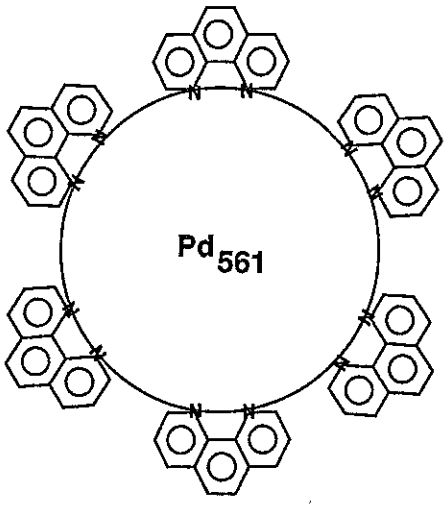

Figure 1.3: Schematic diagram of Pd_{561} cluster.

with a slightly different ligand shell [8] based the proposed structure on molecular weight measurements, EXAFS studies, SAXS (Small Angle X-ray Scattering) analysis as well as TEM (Transmission Electron Microscopy) and NMR (Nuclear Magnetic Resonance) work. In both the studies cited [17, 8], it was recognised that closed shell clusters have a particular stability associated with them, and the nearest closed shell, given the molecular weight, consisted of 561 atoms. It was proposed that the atoms were packed in an icosahedral manner as bond length data from EXAFS suggested this. It was found that the stoichiometry of the cluster was quite varied; SAXS results [8] showed a polydisperse system with cluster cores ranging in size from around 10Å to more than 40Å. The mean of the particle size corresponds roughly to the Pd_{561} formulation. The polydisperse nature of this cluster has raised the question of whether it is a true metallic cluster, or simply a colloidal system.

Work continues in this area, driven in part by the possible applications of this particular cluster as a car exhaust catalyst.

Chapter 2

EXAFS Theory and Analysis

2.1 Theory

2.1.1 Basic Physics

When X-rays pass through a medium they are attenuated by several independent processes such as pair production, inelastic scattering and Auger electron production. All of these processes contribute to the overall shape of an X-ray absorption edge. We will concern ourselves initially with photoelectric absorption, the process which gives rise to the Extended X-ray Absorption Fine Structure (EXAFS) phenomenon. When absorption occurs, the energy of the incoming X-ray photon is used to promote a core electron of the target atom to a continuum state, resulting in a free photoelectron of energy E_f where:

$$E_f = \hbar\omega - E_b \tag{2.1}$$

E_b being the binding energy of the electron and ω the frequency of the X-ray photon. The wavefunction of the ejected electron propogates out through the central atomic potential and, in a condensed sample or molecular gas, is scattered by the potentials of neighbouring atoms, returning to the core atom. This process is depicted in a simplified form in Figure 2.1 where the outgoing and reflected photoelectron waves are depicted as spherical waves.

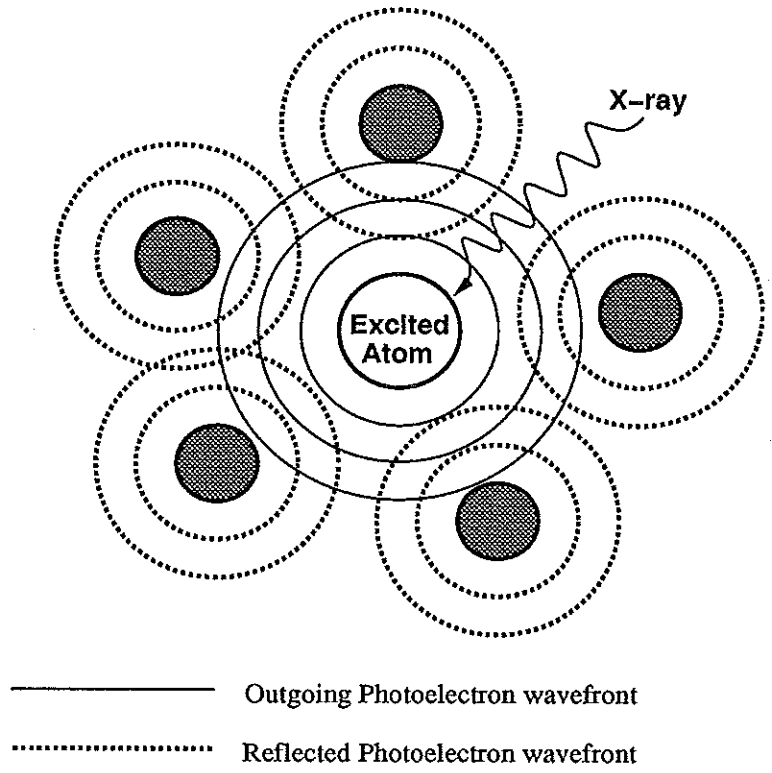

Figure 2.1: Simplified EXAFS process

The way in which the photoelectron moves through the potentials of the central

and backscattering atom, and hence the scattering process itself, is governed by the potential experienced by the ejected photoelectron. The potential model used in the theory discussed here is the Muffin-Tin potential[32] commonly used in solid state physics, which consists of a roughly exponential function close to the atom centres, and a flat potential between neighbouring atoms (See Figure 2.2).

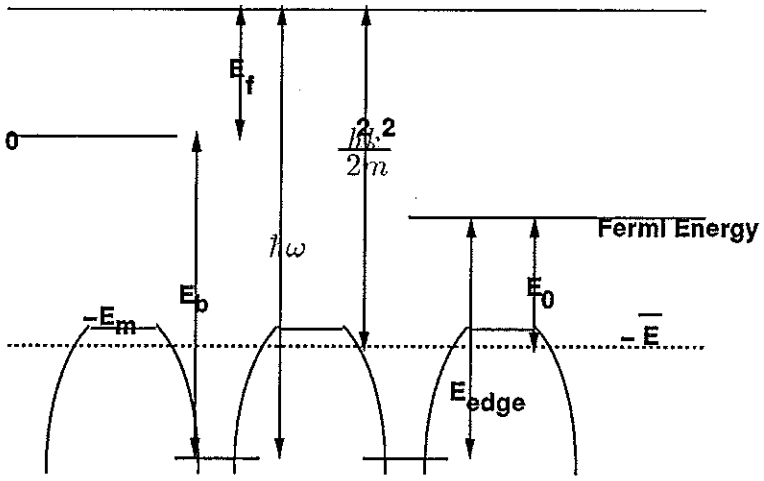

Figure 2.2: Shematic diagram of the Muffin-Tin potential scheme

In this diagram $\frac{\hbar^2 k^2}{2m}$ is the final energy of the ejected photoelectron far above the edge (equivalent to that of a free electron), E_b the (positive) binding energy of the electron in its initial state, $\bar{E}$ the energy of a free electron of zero momentum, E_{edge} is the minimum energy at which absorption occurs, E_0 being the difference in energy required to 'knock out' an electron from the Fermi level. The threshold energy, E_0 is particularly important as it represents a purely arbitrary energy from

the mean electron energy to the Fermi level. This presents problems, but is also useful, as its indeterminate nature allows it to be used to counteract one of the problems encountered in the analysis of EXAFS data, namely the variation in the phaseshifts due to differing chemical environments. The fine structure which appears on the high energy side of the X-ray absorption edge occurs as a result of the modulation of the absorption coefficient of the material under examination, which is a direct result of the interference process described above.

The nature of this interference depends on the atomic type, local atomic density (i.e. mean coordination number), and the distance from the excited core atom to the nearest neighbours. Thus, after applying corrections for the phase shift experienced by the photoelectron during its passage through the atomic potentials, the absorption coefficient of the sample can be related to structural information such as near-neighbour distances, coordination numbers and in addition, chemical types. The probability of photoelectric absorption, P, for a K-edge electron is given by the dipole approximation rule:

$$P = \frac{2\pi^2 e^2}{mc^2\omega} |< f \mid \epsilon \cdot r \mid i >|^2 \rho(E_f) \tag{2.2}$$

where r and ε are the vectors associated with the orientation of the lattice and the beam polarisation respectively, $\mid i >$ is the initial state photoelectron wavefunction, and $< f \mid$ the final state. Far above the edge, the density of states $\rho(E_f)$ is a smooth function of k, i.e. that of a free electron. All of the parameters in this equation remain

constant, except the final state of the photoelectron.

Curved Wave Theory

The EXAFS phenomenon is therefore a final state process, and its exact mathematical description is extremely complex, partly because the outgoing photoelectron gives rise to many backscattered waves, with various components of angular momentum, and also because of the exact treatment of the outgoing wave as spherical - giving rise to the term Curved Wave (CW) theory. As this calculation is mathematically involved, discussion of it is beyond the scope of this thesis. A detailed summary of the full Curved Wave theory may be found however in the work of Lee and Pendry[33].

Fast Curved Wave Theory

For amorphous or polycrystalline systems , the beam polarisation vector ε (or equivalently the lattice orientation vector, r) is spherically averaged, leaving only the diagonal elements of the absorption matrix used to calculate $\mu(E)$. The exact form of the absorption coefficient is then significantly simplified. This equation can be solved exactly using analytical techniques yielding a form of the absorption coefficient that gives the same results for polycrystalline or amorphous samples as the full CW theory. This theory is known as the fast curved wave (FCW) theory[34] and is central to the data analysis procedure adopted here.

2.1.2 A Brief History of EXAFS

The fine structure that occurs above the X-ray absorption edge of a material in its condensed state was first noticed by Fricke and Hertz in the 1920's. The near edge structure that occurs was explained by Kossel initially, but the EXAFS region occurring further beyond the edge (to several hundred eV) requires a different theoretical approach. Kronig's attempt in the 1930's used the then newly developed Quantum Mechanics together with a formulation based on the band gaps between Brilliouin Zones: the so called Long Range Order (LRO) theory. Although fundamentally wrong in conception (as it is now known that the major contribution to the absorption matrix element comes from regions of space very close to the nucleus of the core atom[35]), problems in understanding the underlying EXAFS mechanism, together with experimental difficulties, prevented a more theoretically sound approach from appearing for another forty years.

Phaseshifts were introduced to take account of the passage of the photoelectron through the atomic potentials (Peterson, 1932)[36], and core-hole and photoelectron lifetimes were introduced (Sawada, 1959)[37], followed by a Debye-Waller factor to account for the smearing of the signal due to static and thermal disorder (Schmidt, 1961)[38].

It was Sayers (1971)[39] who realised that a Fourier transform of the EXAFS function with respect to the photoelectron wavevector gives a form of pair distribution

function, which can be used to visualise coordination shells and extract information about bond lengths and Debye-Waller factors. Furthermore this proved the viability of the SRO theory as the radial distribution function showed only the first few coordination shells clearly. The advent of the Synchrotron many years later reduced the time taken to perform experiments from weeks to hours, and introduced the possibility of studying many (e.g dilute) systems that were not previously practicable.

Sterns[40] original treatment of EXAFS, which represented the outgoing photoelectron as a plane wave, led Lee and Pendry[33] to give a detailed account of the EXAFS process in the mid 1970's allowing for the spherical nature of the outgoing photoelectron waves, something which was also achieved by Ashley and Doniach using a Greens function formalism[41]. A variant of the Curved Wave theory was later used by Gurman *et al.*(1988) to form the now widely employed Fast Curved Wave theory[34].

EXAFS is now used to study a broad range of materials in the condensed state with the important advantages of element specificity that is lacking in other experimental techniques such as X-ray diffraction. Furthermore, EXAFS is ideal for the study of biological systems such as proteins, which contain very small proportions of certain elements.

Variants of the EXAFS technique include the more theoretically involved XANES

which uses the same experimental arrangement but involves calculating multiple scattering paths for the photoelectron. This is used in, for example, biological systems where colinear arrays of atoms are common, resulting in the so-called focusing effect whereby the photoelectron is strongly forward scattered.

2.1.3 The EXAFS Equation

In order to describe the various parameters involved in EXAFS, a simplified form of the general EXAFS equation, known as the plane-wave approximation (PWA), will be used here. This is equivalent to Stern's original treatment of the EXAFS process, and results from using the asymptotic limit of the Curved Wave formalism. This is identical to the assumption that for sufficiently high X-ray energies, the outgoing photoelectron can be represented by a plane wave function (a simple exponential), as opposed to the more mathematically involved Hankel functions that are needed in the exact CW theory.

The EXAFS function can be extracted from the raw absorption spectra by use of the following normalisation equation:

$$\mu(E) = \mu_0(E)(1 + \chi(E)) \tag{2.3}$$

where μ_0(E) is the absorption coefficient due to a single isolated atom, and χ(E) is the EXAFS function itself (The actual method of normalisation is considered more carefully in the analysis section).

Once isolated from the background, the EXAFS function can be represented by the following empirical expression:

$$\chi(k) = \sum_{i=1}^{n} A(k)\frac{N_i}{kR_i^2}\sin(2kR_i + 2\delta(k) + \psi_i(k)) \mid f(\pi,k) \mid e^{-2\sigma_i^2 k^2} e^{-2R_i/\lambda} \qquad (2.4)$$

where:-

χ(k) is the normalised EXAFS function.

δ is the phaseshift experienced by the photoelectron upon leaving and returning to the central atom (hence the factor of two);

ψ is the phase shift due to interaction of the photoelectron with the electron cloud of near neighbours;

f(π,k) is the photoelectron backscattering factor;

λ is equivalent to the mean free path of the photoelectron;

A(k) is a correction factor which takes into account processes which do not give rise to EXAFS ('shake up/off' processes), e.g. secondary electron production, inelastic scattering, etc; and

σ^2 is the standard Debye-Waller factor , and is a linear combination of thermal and static smearing of bond lengths.

The photoelectron wavevector is given by

$$k = \sqrt{2m(E - E_0)}/\hbar \qquad (2.5)$$

where E_0 is the threshold energy.

N_i is the number of atoms occupying the ith shell at radius R_i

A 'shell' here has a somewhat arbitrary definition, but is usually used to describe those atoms, of a particular atomic type, that give rise to a distinct and separate (i.e. resolvable) peak present in the partial radial distribution function. It is therefore analogous to the coordination sphere around the central (in this case excited) atom.

The PWA assumes that the peaks in the pair distribution are Gaussian in shape, with a mean square variation in bond distance σ^2. The Debye-Waller and inelastic terms are empirically determined by fitting to the data. This theory is not generally used to analyse EXAFS data, because it models only poorly the scattering contributions near the edge (which are very important, especially for light atoms which scatter low energy electrons more), but allows one to look at the various parameters that contribute to the overall EXAFS spectrum. Other approximations to the full CW theory have been developed. These include the small atom approximation (SAA), also by Gurman[42] which again assumes a plane wave form of the photoelectron wave, but corrects for the phase shift at the atom core, working best at high energies, and of course small atoms. The Fast Curved Wave theory[34] is computationally much less complicated (hence quicker) than the full CW theory, and is used in the EXCURV90 package (see data analysis section)

2.1.4 Phaseshift Transferability

Before proceeding with the analysis of EXAFS data, it is necessary to consider several aspects of the phenomenon qualitatively. Firstly, it is important to note that the backscattered photoelectron waves are not reflected in the classical sense, but experience a phaseshift due to the interaction between the photoelectron and the atomic potentials of the core excited atom and the neighbouring atoms. The phaseshifts are dependent on the photoelectron energy and are denoted $\delta(k)$ and $\psi(k)$ respectively for core and neighbouring atoms. The photoelectron experiences the core atoms phaseshift twice - once leaving and again upon returning. The phaseshifts can be calculated from first principles, but are somewhat dependent upon the local environment of the atoms, therefore the accuracy of the phaseshifts can be tested by using them on a calibrant of known structure, ideally with the core atom in a similar chemical environment. Variation in the bond distances obtained using the calibrant gives a good indication of the accuracy that can be expected using the theoretical phaseshifts. The transfer of phaseshift parameters between samples needs to be done with great care, and particular attention needs to be paid to the reference sample chosen; references with a substantially different chemical environment to the chosen system under study will be much less useful in determining the accuracy of the phaseshifts used. Transferability of phaseshifts remains one of the more widely disputed aspects of EXAFS analysis, with opinions differing as to whether phaseshifts can be calculated for a

reference sample of widely differing environment and successfully transferred. Some authors [43] believe that phaseshifts can be accurately transferred from molecules of a very different chemical environment, but generally a more cautious approach is used e.g [44]. It is the opinion of the author here that, whilst it is advisable to be judicious about the use of phaseshifts, it must be assumed that to a large extent, transferability is a viable procedure. As an indication of the measure of reliability of the phaseshifts, the empirically determined bond lengths for the model compound are quoted alongside those of the unknown.

2.1.5 Attenuation processes

It has already been mentioned that there are several competing processes which take place during an EXAFS experiment which effectively reduce the overall intensity of the EXAFS spectrum. These factors need to be taken account of before an accurate model of the spectrum can be generated. There are three main non-EXAFS processes included as empirical reduction factors in the PWA equation.

- Inelastic Scattering.

  The inelastic scattering of the photoelectron by neighbouring atoms is represented by a damping term $e^{[-2r_j/\lambda_j(k)]}$, where r_j and λ_j are the distances from the core atom to the neighbouring atoms, and a mean free path term respectively. The mean free path here is actually a combination of the inelastic scattering

experienced by the photoelectron (which does *not* contribute to the EXAFS process) and the lifetime of the excited core-hole, both of which are found to be energy independent[35]. This leads to a square root variation in the mean free path with respect to energy, i.e. inelastic scattering in more important at lower k values.

- Shake up/off processes at the core atom.

  Shake up and shake off effects also play an important role in the analysis of EXAFS. Both processes occur at the core atom and are associated with excitation to a bound state and a continuum state (i.e. ionization) respectively. As quantum mechanics dictates that the total X-ray absorption must remain constant (from equation 2.2), multiple excitation effects such as this will reduce the overall EXAFS signal, and need to be taken into account otherwise apparent coordination numbers will be reduced significantly.

  There are two main contributions to the shake up/off processes. The presence of 'passive' electrons, which do not directly take part in the scattering process but are excited along with the photoelectron, alter the atomic potential as seen by the ejected photoelectron. This is because the shielding of the nucleus by the core electrons has been reduced by one electron resulting in the outer electrons perceiving an effective nuclear charge of Z+1, leading to an atomic rearrangement.

Similary, the excess energy can be used to promote a secondary electron from a valence shell, as shown in Figure 2.3

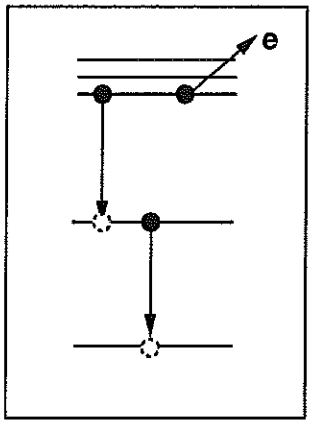

Figure 2.3: Secondary electron production

Both of these effects are important close to the absorption edge, as the potentials of the ejected photoelectron and core hole are spatially close to one another for a significant time, reducing the overall EXAFS signal.

- Structural and thermal disorder.

  The vibrational and static structural disorder of a system also has to be taken into account when attempting to represent correctly the EXAFS process in a mathematical form. If the core atom is vibrating, then its position may alter between the emission and recapture of the photoelectron. This results in a smearing of the EXAFS signal due to the uncertainty principle, and a broadening of the peaks in the Fourier transform. Likewise, as the overall signal is averaged over the entire system, local static disorder due to variation in near

neighbour separations will also occur, and is included in a single parameter, which is the standard Debye-Waller factor of the general form $e^{-2\sigma^2 k^2}$. This comes from the assumption that the peaks in the radial distribution function of the system are Gaussian in shape (see Section 2.). The components of local thermal vibrational disorder and static structural disorder can be separated if several EXAFS experiments are taken at sufficiently different temperatures, e.g if, for instance, measurements are taken below the Debye temperature (below which mostly static structural disorder dominates) and at room temperature. If thermal and static structural contributions are assumed to be independent, then vibrational effects can be calculated from the following formula:

$$\sigma^2_{total} = \sigma^2_{thermal} + \sigma^2_{static} \tag{2.6}$$

The vibrational component of the Debye-Waller factor does not relate to the absolute vibrations of atoms however, but is to some extent correlated to nearest neighbour vibrations, i.e. vibrations of the core atom are relative to the neighbours present. The reason for the Debye-Waller smearing of the EXAFS function is that there is an uncertainty in the position of the core atom or the backscatterer during the time in which the photoelectron is propagating outwards and back. This is to be contrasted with X-ray diffraction data which gives *absolute* magnitudes of this type of disorder.

2.2 Summary

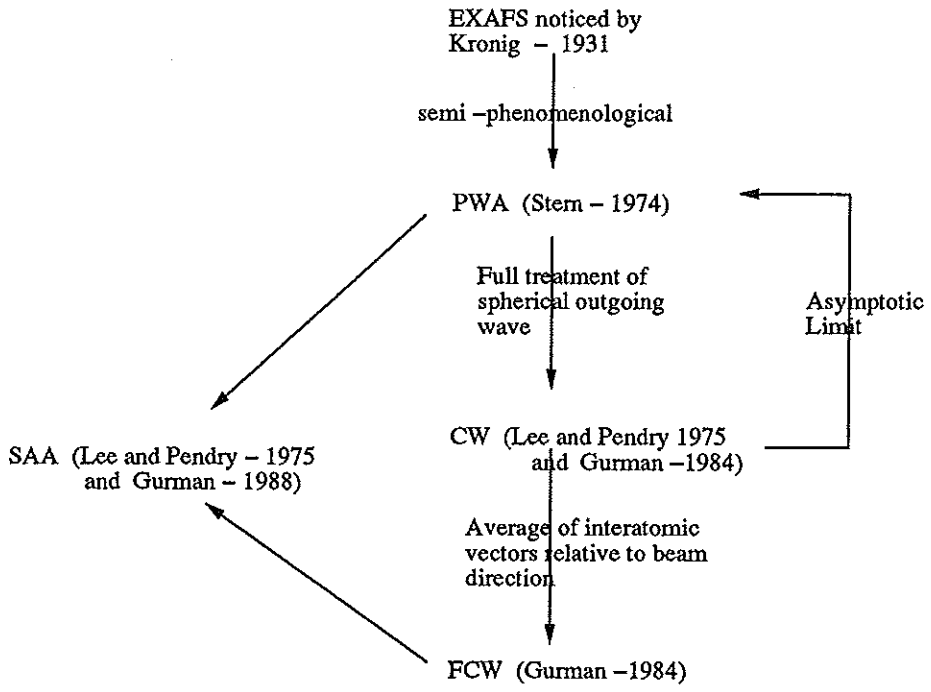
EXAFS noticed by
Kronig – 1931
semi –phenomenological
PWA (Stern – 1974)
Full treatment of
spherical outgoing
wave
Asymptotic
Limit
CW (Lee and Pendry 1975
and Gurman –1984)
SAA (Lee and Pendry – 1975
and Gurman – 1988)
Average of interatomic
vectors relative to beam
direction
FCW (Gurman –1984)

2.3 Data Analysis

Given the high level of current understanding of the theory of the EXAFS phenomenon, much of the work now necessary by the experimentalist is focusing on the refinement processes necessary to extract the EXAFS function from the raw data, shown in Figure 2.4, and glean more accurate results from it. In this section the major points to be considered are :-

1. Normalisation.
2. Weighting Scheme.
3. Fourier Transformation.
4. Fitting procedure.

2.3.1 Background Subtraction and Normalisation

The background subtraction and normalisation of EXAFS data can cause severe problems in the later stages of analysis if it is not carefully considered. The objective of the normalisation process is to to remove underlying contributions from lower X-ray edges, and ensure that the EXAFS oscillation occurs about a uniform intensity level free from the decay physically corresponding to that experienced by an isolated atom, which would give a smooth absorption coefficient $\mu_0(E)$. The EXAFS function, $\chi(E)$, can be defined in terms of the total absorption coefficient $\mu(E)$ by rearranging

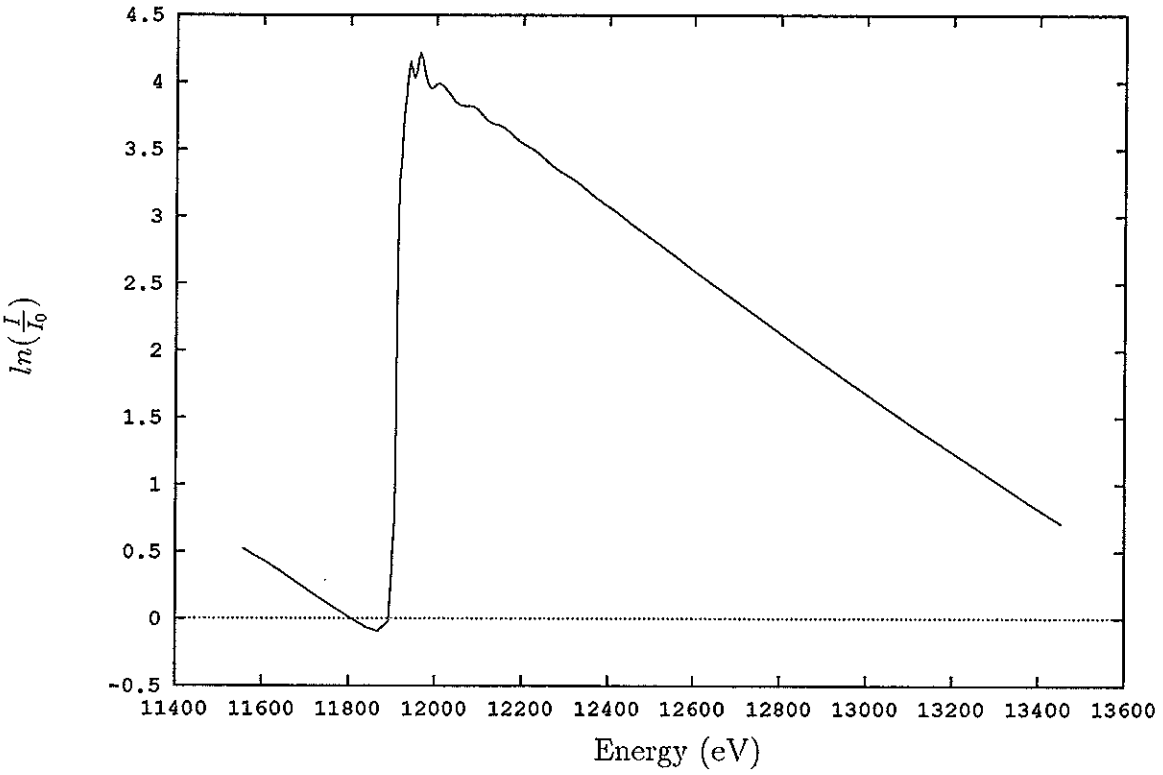

Figure 2.4: Raw EXAFS Spectra, taken in transmission mode, of the L(III) edge of gold foil

equation 2.3 we obtain:-

$$\chi(E) = (\mu(E) - \mu_0(E))/\mu_0(E) \tag{2.7}$$

Transformation from E to k is achieved through use of equation 2.8, which links the wavevector k to the threshold energy E_0 and the X-ray photon energy E.

$$k = \frac{\sqrt{2m(E - E_0)}}{\hbar} \tag{2.8}$$

To allow for the chemical dependence of the phaseshifts and amplitude reduction factors, E_0 is allowed to float freely during the iteration procedure, equalizing any slight perturbations. At this stage it can be seen that, as k is dependent upon E_0 and the R values are dependent upon k, R is intrinsically linked to E_0. Similarly coordination numbers and Debye-Waller factors are related to the chemical dependent reduction factor A(k). This is important during the data analysis as correlated parameters are varied together during the fitting procedure.

For successful background removal it is necessary that the oscillation of μ_0(E) is of a significantly lower frequency than the fine structure oscillations, which is nearly always the case. The three main stages of normalisation are illustrated in Figure 2.5 and usually involve fitting and then removing the pre-edge with a simple polynomial (a), subtracting the pre-edge polynomial from the oscillatory part of the spectrum (b), and finally fitting a series of splines or polynomials to the post-edge region, isolating the EXAFS itself (c).

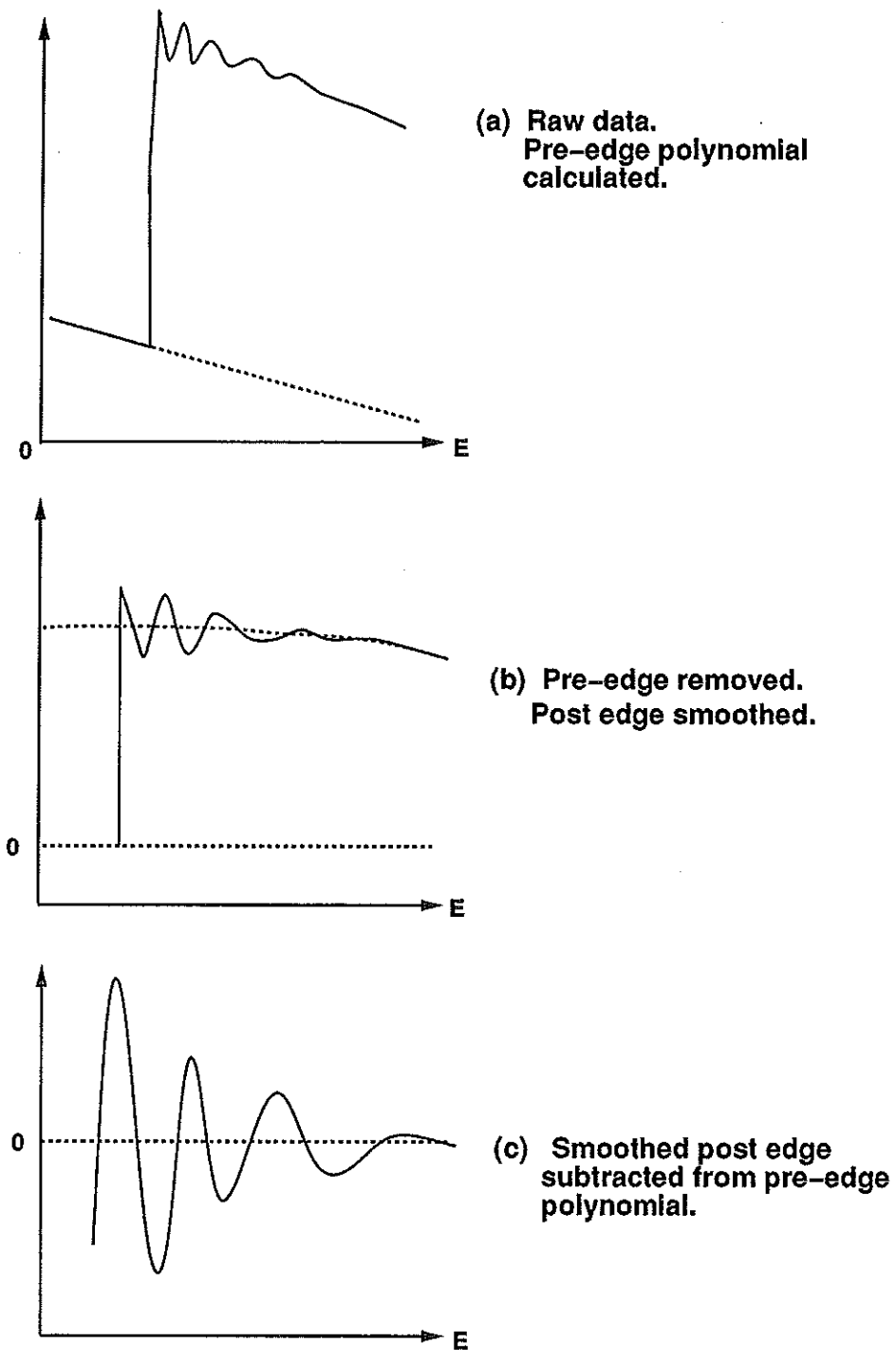

Figure 2.5: Normalisation stages

If some of the background oscillation still remains, or if an additional trend is introduced through bad curve fitting, then the Fourier transform will contain unphysical or spurious features, often at low r which, even if filtered correctly, can affect the main peak under study, and hence the derived coordination numbers and bond distances. The effect of poor fine structure isolation is shown in Figure 2.6

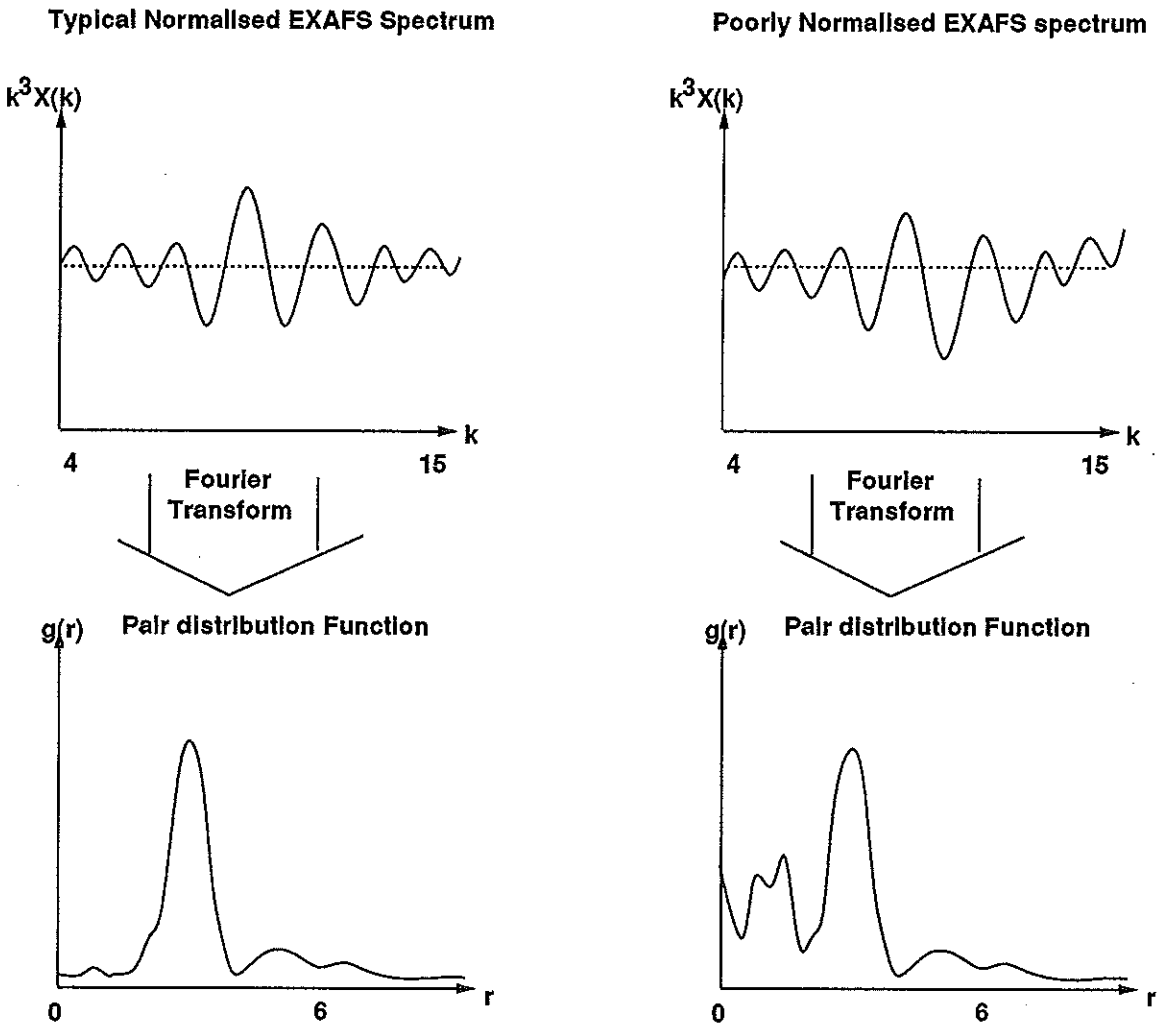

Figure 2.6: Effect of poor normalisation on low R content of Fourier transform

In the method used here, normalisation proceeds as follows:

- Energy Scale Calibration. The edge energy is first selected, usually by taking the point of maximum gradient of the absorption coefficient. As mentioned before, the threshold energy, E_0, will vary in the fitting procedure, so selection of zero energy is not of vital importance here. To ensure that the edge position selected is reasonably close to that of the spectrum, a value of the pure element is used (i.e. for Au L(III) edge $E_{edge} = 11.918$KeV).

- Glitch removal. Absorption data will often contain spurious background 'spikes', caused by instrument noise and harmonics in the X-ray beam (which create data spikes when interference with the monochromator occurs). This necessitates the explicit removal of any obvious 'spikes' before proceeding with data analysis, as sharp peaks will give rise to unphysical features in the Fourier transform. It is of course advisable to be cautious about removal of suspect peaks near the edge, as these may be a part of the XANES structure.

- Removal of pre-edge. To remove the contribution of lower edges and the effect of Compton scattering, a simple polynomial of the form:

$$y = mx + c \tag{2.9}$$

is fitted to the pre-edge. Other methods include the use of the Victoreen function, which is an empirical expression of the form:

$$C_1\lambda^3 - C_2\lambda^4 \tag{2.10}$$

which is not used here to avoid converting to λ, the incident photon wavelength. Either method will suffice, as the pre-edge has a linear trend within the data range used.

- Post-edge background removal. As stated previously, the aim of successful normalisation is to remove any slow underlying trends in the absorption coefficient. The method used here involves heavily smoothing the post edge region. This fits a line through the original EXAFS oscillations whilst removing the lower frequency trends. The almost ubiquitous first post-edge peak is problematical here, as this relatively sharp feature greatly complicates the smoothing procedure, and is thus ignored: data smoothing starts at around 25 data points beyond the edge depending on the data set. At this point it is important to check graphically that :

  (a) the smoothing parameter is sufficiently high enough to ignore fine structure oscillations, and

  (b) the smoothing begins far enough past the edge for the near-edge features not to affect the smoothing curve.

To indicate how selection of the smoothing parameter affects the quality of the results, Figure 2.8 and 2.7 show the result of high and low smoothing parameters overlayed onto the raw data set (after the pre-edge has been removed). In Figure 2.7, it can be seen how the EXAFS oscillations are being followed by the fit, and consequently reduced in intensity. The effect of this bad smoothing is shown in Figure 2.9, which shows the reduced intensity of the Fourier transform compared to that of a good fit. The example chosen is that of colloidal gold. Not only does the poorly smoothed data have a reduced first peak height, but the fit index for these data is markedly higher (i.e. gives a poorer fit) than the correctly smoothed data. Although the smoothing parameter tends to affect only low R values, usually just the first peak in the Fourier transform, this is still important as much of the work performed using EXAFS is primarily concerned with this first peak (also it may contain contributions from shells of differing atomic types (see results chapter)).

- Normalisation. Once satisfactory smoothing has been achieved, normalisation can proceed through use of equation 2.3 as before.

As normalisation of the data presented here was not performed using standard software, it was useful to compare results achieved using the routine adopted for this work ('SMOOTHED') and those using EXBACK. An illustration of the difference in the Fourier transform after using the two methods is shown in Figure 2.10 using Pd_{561}

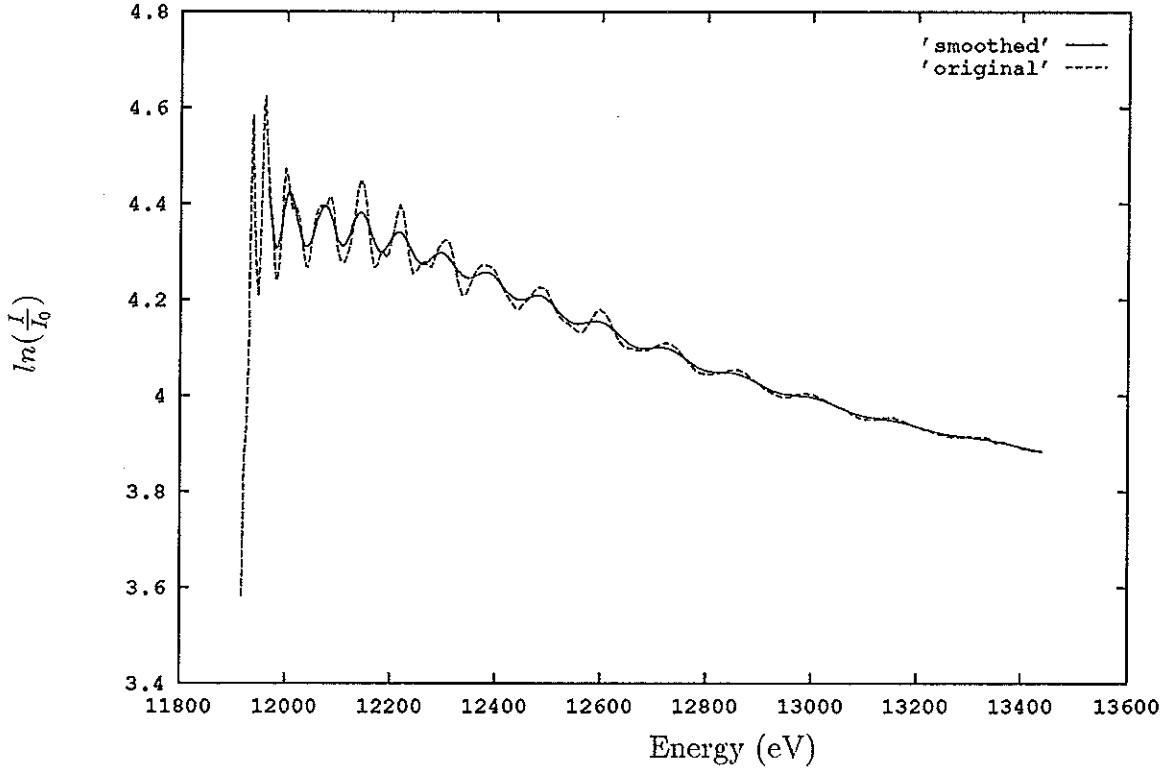

Figure 2.7: Poorly smoothed

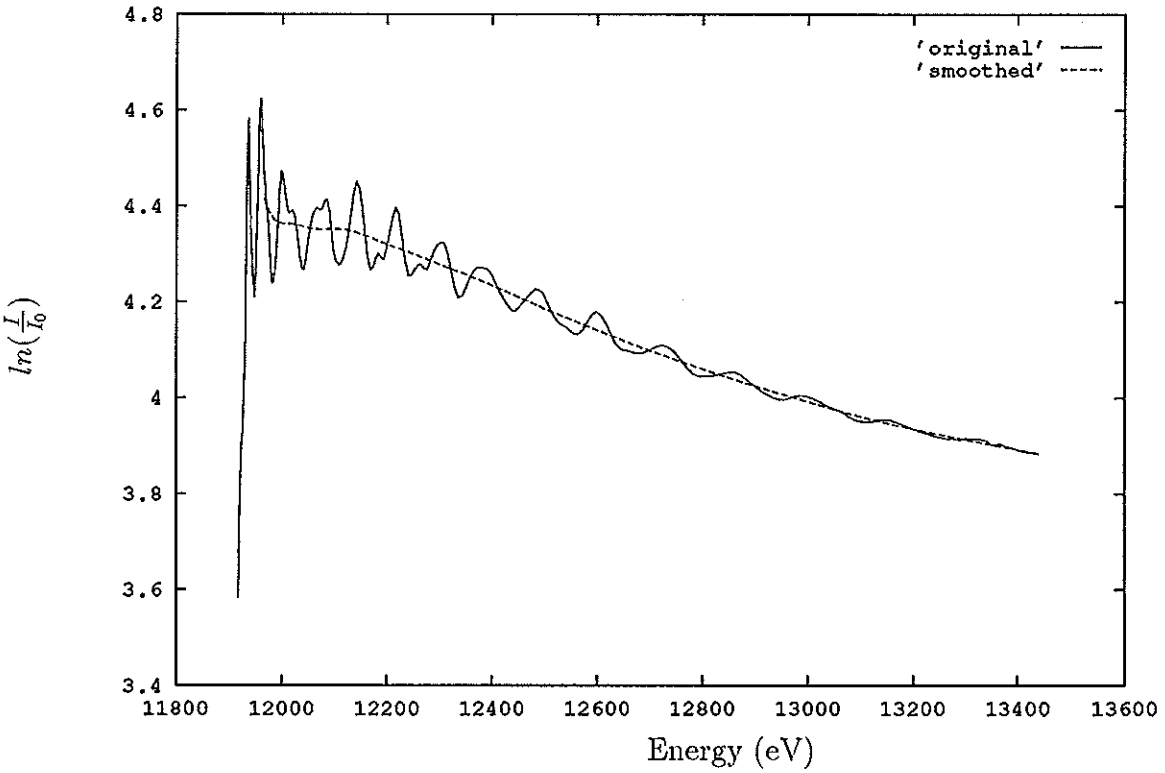

Figure 2.8: Correctly smoothed

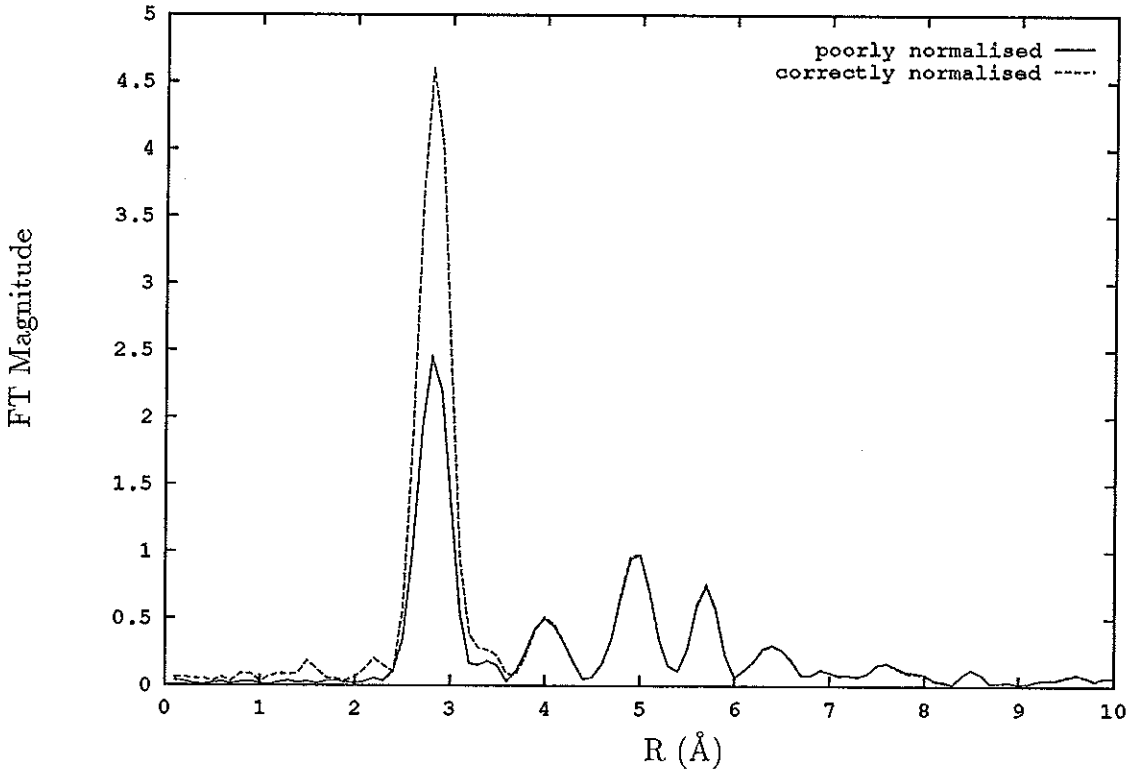

Figure 2.9: Fourier transform of previous data, showing reduced intensity due to poor smoothing

as an example. This shows that the smoothing method generates less noisy results, and gives much the same fit-parameter results as EXBACK (bond distances varied by less than 0.001Å and coordination numbers and Debye-Waller factors by less than the standard errors quoted by EXCURV90), whilst reducing drastically the amount of time used in EXBACK to select manually polynomial intersection points on the post edge.

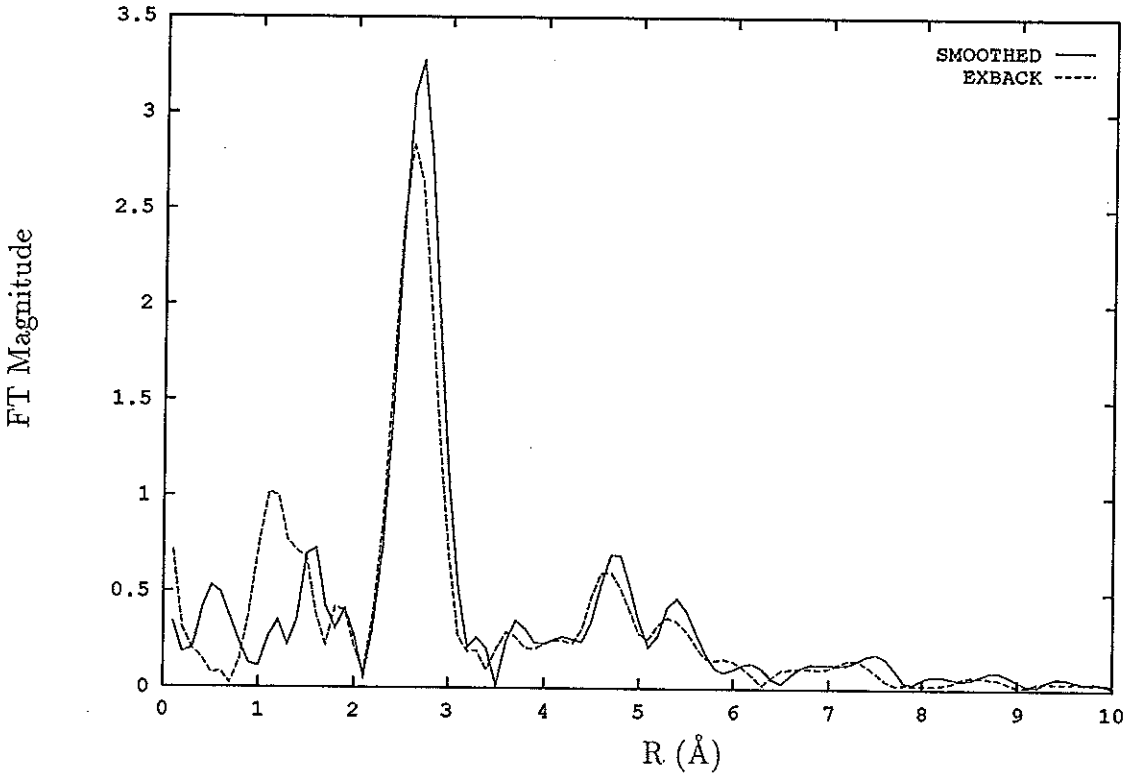

Figure 2.10: Comparison of Normalisation techniques

For a more detailed treatment of normalisation, including the technique used here at UKC[45], several authors include chapters on this subject[46, 47, 45]

2.3.2 Weighting

The EXAFS signal is usually given a weighting factor, generally k^3, before Fourier transformation is applied. There are several reasons for this.

Firstly it counteracts the 1/k dependence of the EXAFS function, which causes attenuation of the signal at high k, resulting in a loss of real-space resolution. Even with weighting schemes, the finite data range of EXAFS will necessarily affect the resolution of the transform.

Secondly, weighting offsets the decay caused by the backscattering function $f(\pi,k)$ of neighbouring atoms.

Lastly, k^3 weighting suppresses the XANES (X-ray Absorption Near Edge Structure) region which is prominent at low k. As has already been mentioned, XANES involves multiple scattering effects which occur in linear or nearly linear arrays of atoms, such as those found in biological systems. In the system studied here it may safely be assumed that XANES effects do not contribute significantly to the scattering processes, and the region close to the edge is not used.

It can be useful when curve-fitting to EXAFS data to obtain first the best fit with k-weighting, then move on to k^2 and finally k^3, as the more prominent low-k region can be fitted first and subsequent higher weighting schemes allow one to concentrate upon the high-k regions.

The effect of various weighting schemes on the envelope of the EXAFS spectrum

are illustrated in Figure 2.11, where a simple simulated spectrum is shown unweighted, k^2, and k^3 weighted. The spectra are normalised to equal intensity at k=2 to highlight the differences.

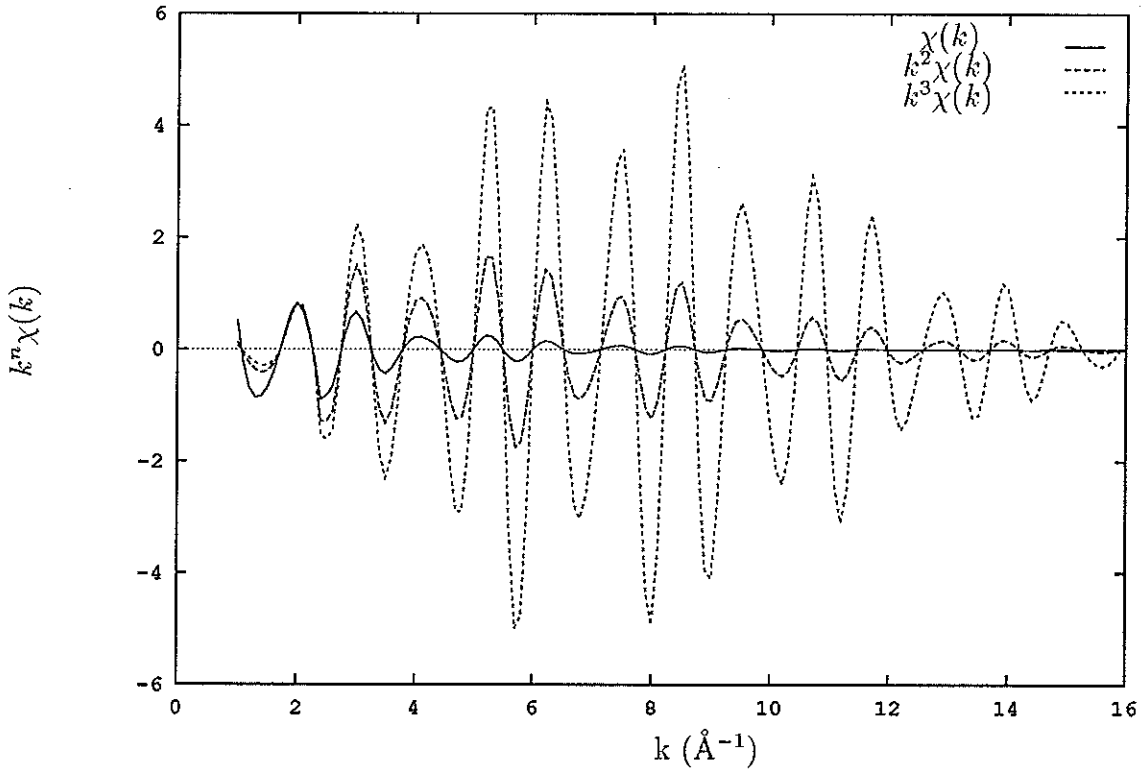

Figure 2.11: Weighting Schemes used.

2.3.3 Fourier Transformation

Sayers et.al.(1971) [39] showed that, as the PWA 2.4 involves a sum over all atom types, one could replace the sum with a pair distribution function $P_{\alpha\beta}(r)$, as this involves a similar summation over the entire system.

The empirical inclusion of the Debye-Waller factor in the PWA shown in equation 2.4 comes directly as a result of the assumption that the pair distribution function of the sample consists of Gaussian peaks with a mean square variation σ_j^2 in bond distance for atoms in shell j.

The Fourier transform of the EXAFS signal with respect to the photoelectron wavevector allows one to visualise coordination shells and can be used to analyse the EXAFS data in r-space. It should be pointed out here that, although the result of the Fourier transform gives a function which resembles a pair distribution function, P(r), the result is actually a **modified** P(r), denoted ρ(r). The definition of ρ(r) can be expressed thus:

$$\rho(r) = \frac{1}{\sqrt{2\pi}} \int_{k_{min}}^{k_{max}} w(k) k^n \chi(k) e^{i2kr} dk \qquad (2.11)$$

where w(k) is a smooth window function such as a Gaussian, used to reduce the truncation ripples resulting from finite data ranges, common in Fourier transformations.

The transform is generally performed with respect to exp(-2ikr) and the modulus taken, as this removes problems of sine transformations, which result in oscillations of frequency π/k_{max}, shown in Figure 2.12.

There are several consequences of transforming to r-space, most of which can be corrected for. The k-dependence of the phase shifts and backscattering factor f(π,k) has already been mentioned. If no allowance is made for these terms when

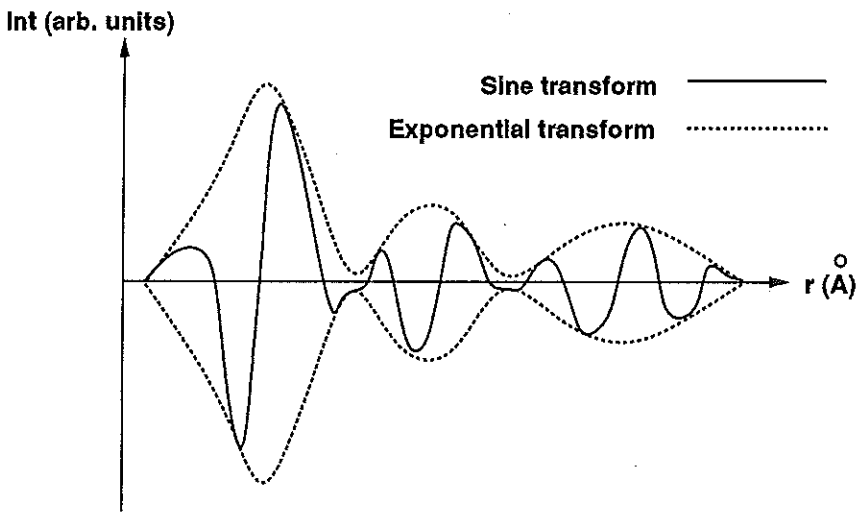

Figure 2.12: Comparison of Sine and Exponential Fourier transforms

transforming the EXAFS function, then the peaks in ρ(r) are shifted. If the phase functions are assumed to be linear, of the form:

$$2\delta(k) + \psi(k) = p_0 + p_1 k \tag{2.12}$$

Which usually holds true (see section 6.8 in Teo[46]), then the peaks will be translated by an amount $p_1/2$, since χ(k) varies sinusoidally as:

$$sin[2kr + \psi(k) + \delta(k)] \equiv sin[p_0 + (p_1 + 2r)k]. \tag{2.13}$$

Transforming with respect to exp(-2ikr-2δ-ψ) and taking the modulus circumvents this problem, and weighting the experimental spectrum with the calculated backscattering functions removes their k-dependence. However, the problem of the finite data range remains, contributing to the small side lobes that appear with the main peaks. Resolution is a problem in crystalline systems as truncation of high k data leads to a

decreased definition in the transform, however amorphous systems tend to have much broader peaks and are thus less prone to resolution problems.

Clearly working with the Fourier transform of the spectra has limitations, but these can be overcome by careful truncation of data, use of the correct window function (a smoothly varying one), and comparison with calibrant samples to ensure that phaseshifts and backscattering functions have been correctly applied. The major application of the Fourier transform is its use as a quick route for gauging the amount of information contained in the EXAFS spectrum, and as a rough guide for bond lengths, coordination numbers, and peaks widths.

2.3.4 Fitting Procedure

EXCURV90

The software package commonly used to analyse EXAFS and XANES data from the SRS, is EXCURV90; all data analysis presented in this thesis has relied upon it. A brief overview of the way in which data is treated within this package is given here, together with a mention of the statistical regularisation procedures implemented; further details are available in the technical manual [48].

The two main methods of EXAFS analysis are k-space, relying on fitting a theoretical EXAFS function to the normalised spectra, and r-space, which uses the Fourier

transform on which to base the fit. Other methods are mentioned in Teo[46]. Although EXCURV90 displays graphically both k and r-space forms of the data, it fits to the experimental spectrum in k-space. The FCW (Fast-Curved Wave) theory is used throughout, but the SAA can be used if multiple scattering is required to be calculated interactively. Several packages form the data analysis software used at Daresbury. These include EXCALIB, used to sum spectra together; PLOTEK, used to display EXAFS spectra graphically at various stages of refinement before complete normalisation; and EXBACK, used to normalise data (which is not used here - see normalisation section).

Analysis of EXAFS data proceeds as follows:

- Addition of several runs on the same sample to improve the signal:noise ratio. Each spectra is viewed graphically before summing to check for any glitches due to electronic spikes, beam inhomogeneity, etc. Glitches can be removed from within EXCALIB if necessary.

- Normalisation is performed[45]. Again, the spectra is checked graphically, here to ensure that the smoothing parameter is not too low resulting in a loss of fine structure intensity.

- The normalised EXAFS spectrum is read into the EXCURV90 package, where it is converted to k-space and weighted appropriately. Examination of a Fourier

transform performed at this stage allows initial estimations of the primary parameters (R,N,A and the atomic type) for the first shell. These values are used as input parameters, and varied interactively until the fit index (FI) between the theoretical and experimental spectrum is minimised. The FI is defined as follows:

$$FI = \frac{1}{100NPT} \sum_{i=1}^{NPT} [(\chi_{i,calculated} - \chi_{i,experimental})k^{wt}]^2 \qquad (2.14)$$

where NPT is the number of experimental data points, and wt the k-weighting as described before.

After the primary feature in the ρ(r) has been fitted, successive shells are modelled in a similar way, until all significant features have been accounted for. If the EXAFS spectra still shows phase and amplitude differences from the fit, then it is probable that atoms of a different mass to that initially assumed to be in the main peak are present in addition. Different atoms give rise to peaks at different places in k-space, Heavier atoms showing more structure at the low-k end of the EXAFS spectra, so are distinguishable even if they occur at similar r-values to the main peak (i.e. lie within the main Gaussian). As an aid to the addition of shells of differing atomic types, EXCURV90 can display graphically the variation in the FI with two correlated parameters as a contour plot. These 'map plots' can display subsidiary minima within a peak, indicating the presence of an additional shell. A typical map plot is shown in figure 2.13.

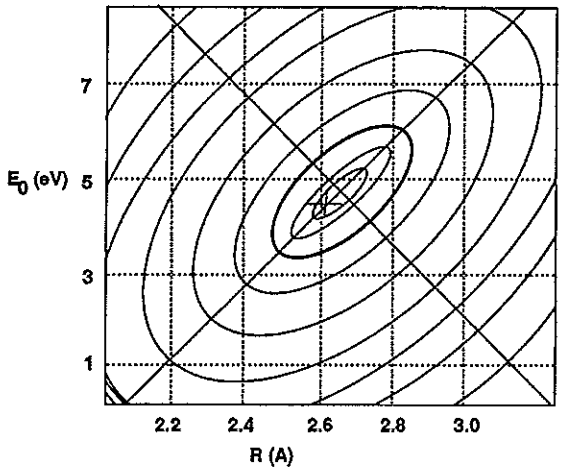

Figure 2.13: Typical Correlation Map Plot

The maps are primarily used to ensure that the current parameters are positioned correctly within the minima of the FI, and not in subsidiary minimum. The disadvantage of the map plot is that only two correlated parameters are varied, whereas during the iteration process, all of the primary parameters are used in calculating the minimum FI. Regardless of this drawback, the maps provide a useful visual aid in EXAFS analysis, and can also be used to estimate the inherent errors in the fitting process (see Joyner et.al[49]).

Statistical Analysis

The fitting of Gaussian peaks to the shells requires a degree of statistical consistency, to ensure that the feature modelled constitutes a real peak, and not spurious noise, or side lobes from other peaks. Consequently, a statistical analysis system is built into EXCURV90. This was developed by Joyner [49], and deals with the problem of whether fitting an additional shell to the data is valid, as fitting more Gaussians to the data will naturally lead to a reduction in the FI regardless of whether the shell is physically significant or not. The criterion for the addition of a new shell is given for 200 data points and up to 10 shells in Joyner *et al.*[49] as:

$$\frac{FI_{n+1}}{FI_n} < 0.96 \tag{2.15}$$

i.e. a new shell must decrease the fit index by at least 4% to be significant. Several implications arise from the use of statistical regularisation , namely:

1. The fitted shell must be taken along with chemical and physical evidence. For example, unreasonably large coordination numbers or Debye-Waller factors give sufficient cause to doubt the validity of the shell, and bond lengths differing widely from those of chemically similar compounds also need to be checked closely before proceeding.

2. When fitting the nth shell, the parameters for all previous shells are allowed to vary.

3. The statistical analysis can only be applied to the *raw* data, i.e. smoothed, and especially Fourier filtered data, do not lend themselves to this procedure, as the analysis assumes that all of the data points are independent.

To estimate the errors incurred by fitting in this manner, the map plots can be used. Plotting two correlated parameters and highlighting the region at which equation 2.15 is obeyed can give the errors associated with the two parameters in question. The error which EXCURV90 returns during the fitting procedure is calculated assuming that the spread of results is Gaussian, and is that of one standard deviation, i.e. 67% of the parameter probability distribution values lie within this confidence region. The highlighted region of the map (present when the statistical regularization procedure is implemented) shows a confidence region of 96%. The latter is the error which is quoted in subsequent results presented here.

Chapter 3

Experimental Details

3.1 Synchrotron Radiation

The advent of Synchrotron radiation has had a dramatic effect on the quality and diversity of experiments being performed with electrons and X-rays. The basis of the synchrotron is quite simple, and relies on the fact that a charged particle will, if accelerated, emit radiation. A standard synchrotron source consists of a linear accelerator which pumps electrons into a booster ring. The booster ring then periodically supplies electrons to the main storage ring which is kept under vacuum. As the electrons circulate within the ring, synchrotron radiation is emitted tangentially, and it is this characteristic, high intensity, focusable radiation which is of interest to the experimentalist. A Schematic diagram of the SRS ring at Daresbury U.K. is shown

in Figure 3.1

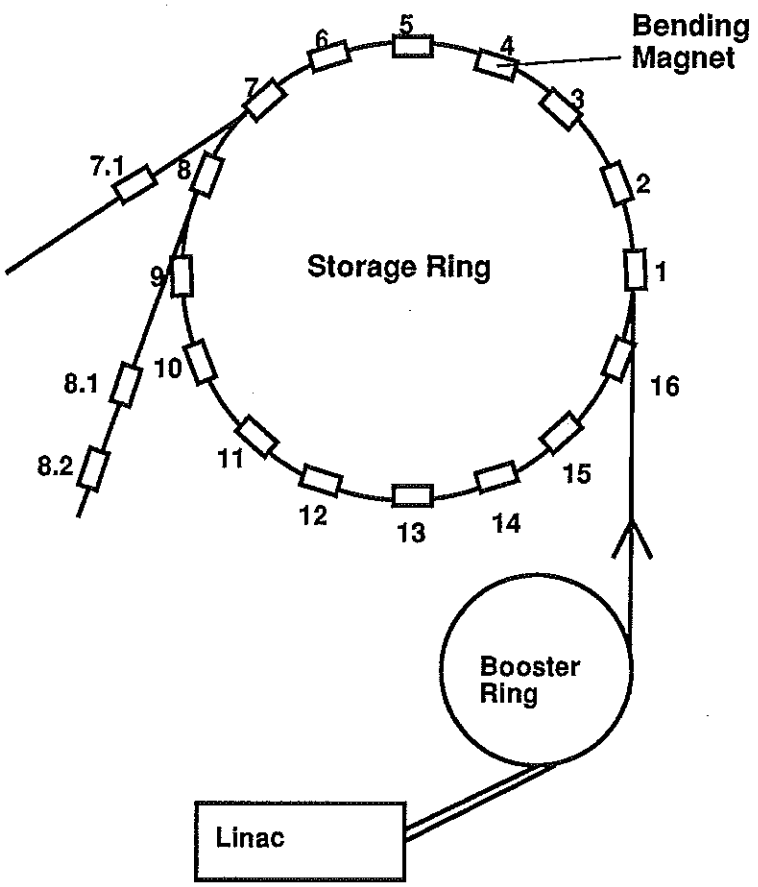

Figure 3.1: SRS Schematic Layout

The requirements of any synchrotron source are primarily those of high intensity and resolution. The Daresbury SRS facility consists of a 10m diameter storage ring enclosing a vacuum at less than 10^{-9} mbar. The ring is formed of sixteen 1.2T bending magnets separated by straight sections. The energy of the beam is approximately 2GeV with a beam current of up to 300mA. Devices known as klystrons replenish the energy lost by the electrons as they emit X-ray photons. The characteristic spectral

intensity distribution of a synchrotron ring can be altered by various insertion devices, which by means of high powered magnets, give the electrons sinusoidal oscillations, forcing them to emit radiation of higher wavelengths: wigglers use high intensity magnets (5T) to produce hard X-rays up to 100keV, and undulators provide increased intensity together with harmonics imposed by the interaction of the electrons with the X-ray photons. The affect upon the characteristic spectral distribution due to the wigglers is shown in Figure 3.2

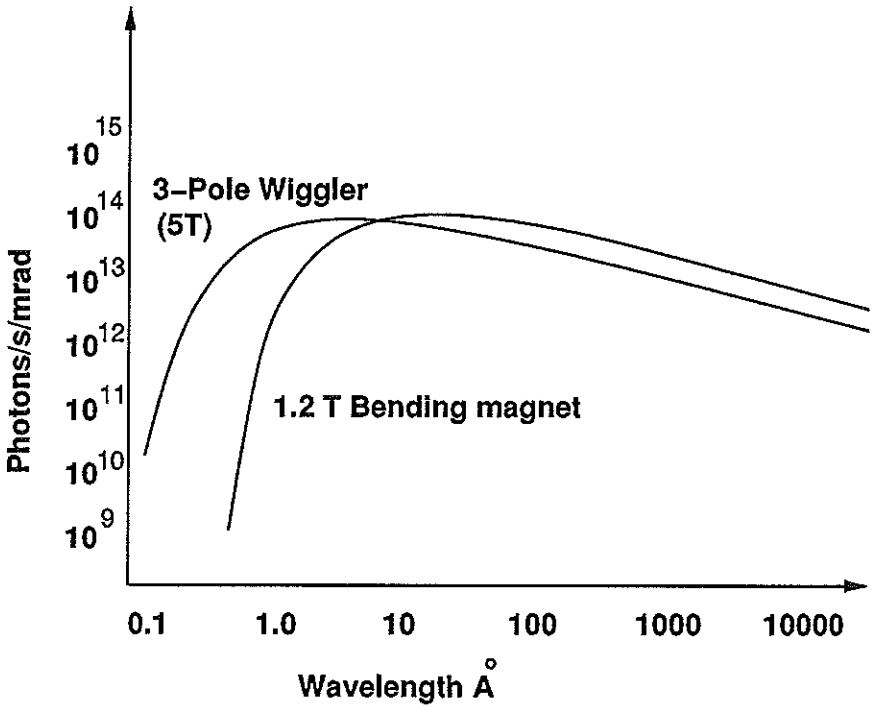

Figure 3.2: Effect of Wiggler on Spectral intensity Distribution

The storage ring will generally require refilling every 24 hours, as beam intensity is lost due to the divergence caused by electron-electron interaction, and the presence of gaseous molecules. Numerous experimental stations or 'beamlines' are positioned

around the ring near the tangents of the magnets. Different stations require varying degrees of beam intensity, wavelength and size, so each station is equipped with devices for monochromation, focusing and detection.

3.2 Beamline Specifications

The data were collected at the SRS synchrotron facility at the Daresbury laboratory, U.K., gold L(III) edge data taken on beamline 7.1 using a Si(111) monochromator crystal, and K-edge palladium data recorded on beamline 9.2 using a Si(220) monochromator.

EXAFS spectra were taken of $Au_{55}(PPh_3)_{12}Cl_6$, $Au_{55}PPh_2(C_6H_4SO_3Na)_{12}Cl_6$, $Au_{11}\{PPh_2(p\text{-}ClC_6H_4)\}_7I_3$, $Pd_{561}(phen)_{36}O_{200}$ and both gold and palladium foil at room temperature and after cooling in a liquid nitrogen jacket to approximately 80K. Several runs were taken for each sample to improve the signal:noise ratio of the spectra.

3.2.1 Beamline 7.1

Beamline 7.1 was set up in transmission mode. The energy range of this station is approximately 4 - 14keV, and uses a double crystal monochromator as illustrated in Figure 3.3.

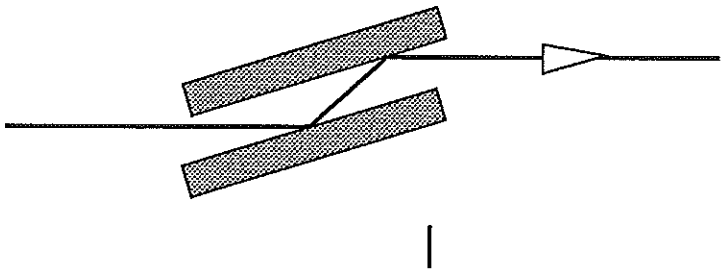

Figure 3.3: Double Crystal Monochromator

Monochromation is achieved through use of the standard Bragg equation governing reflection of X-rays by a crystal lattice:

$$n\lambda = 2d\sin\theta \tag{3.1}$$

where n=1 for first order harmonics, d the spacing of the planes between the crystal lattice, and λ the wavelength allowed to pass through. One of the advantages of a double crystal monochromator is that by offsetting one of the crystals, second and higher order Bragg reflections which result in several different wavelengths being incident on the sample, can be reduced dramatically. The focusing mirror used for this beamline is coated with Pt, as its high electron density allows one to use a higher critical angle of incidence for total external reflection to occur. The horizontal and vertical limits of the beam entering the monochromator are constrained by entrance slits, whilst exit slits vary the size of the beam incident on the sample. The monochromator itself together with the slits are kept under a rough vacuum to reduce air scatter, having a beryllium window separating this arrangement from the rest of the beamline, open to air. The beam position was determined using X-ray sensitive paper.[50]

3.2.2 Beamline 9.2

Whilst similar in arrangement to beamline 7.1, a wiggler is present on this line (line 9), giving the increased intensity at higher energies necessary for the higher energy Pd edge (24.35KeV). A Si(220) monochromator is used here giving a theoretical energy range of 3.3 - 18.6KeV for 80-10° Bragg angles. [50]

There are three main ways in which to measure the EXAFS coefficient, μ(E) experimentally:

- Transmission. Here the absorption coefficient is measured directly as a ratio of the incidence to transmitted X-ray photons, the absorption coefficient extracted using the expression:

$$\mu_{total}(E)t = ln\frac{I_0(E)}{I_t(E)} \tag{3.2}$$

Where μ_{total} is the total absorption coefficient of the sample, t its thickness and I_0 and I_t the incident and transmitted X-ray intensities respectively. Both intensities are measured using ion chambers - cylinders containing a mixture of gases confined between two beryllium windows (through which the X-rays pass). These are used to calculate the intensity of the X-ray from the magnitude of the photo-ion current created when an X-ray passes through the gases present in the chamber.

The arrangement of a standard EXAFS experimental beamline in transmission mode is shown in Figure 3.4.

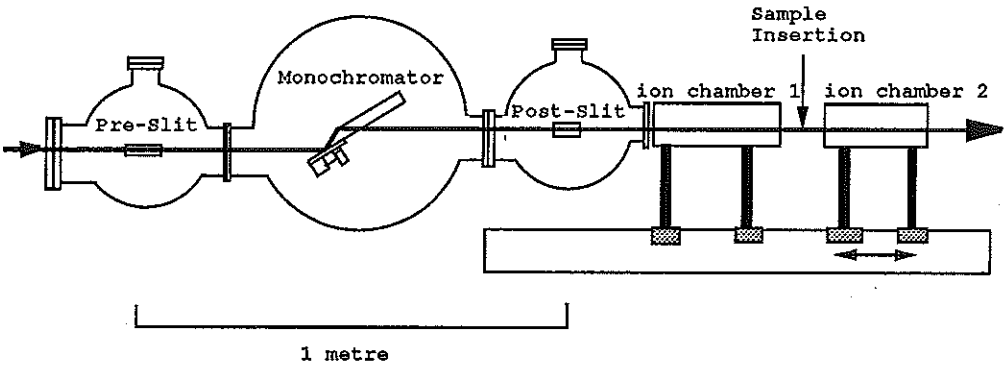

Figure 3.4: Typical transmission EXAFS beamline set-up

The mixture of gases within the chamber required for the correct attenuation of the beam is calculated prior to running an EXAFS experiment. The ion chambers for the gold samples used an argon/helium mixture on beamline 7.1 whilst those for the palladium samples used a krypton/helium mixture on beamline 9.2. The ion chambers serve two purposes here, that of allowing for fluctuations in the overall beam intensity, and also of attenuating the beam for optimum performance (necessitated by the finite number of photons available). The latter requirement can be calculated using statistics: If the fraction of the beam lost in determining the incident intensity , I_0, is f, then the transmitted intensity will be $(1\text{-}f)e^{-\mu t}I_0$, giving the *actual* measured ratio as :

$$R = \frac{(1-f)}{f}e^{-\mu t} \tag{3.3}$$

From this the statistical noise can be derived, and thus the optimum values of f and μt required (f=0.24 and μt=2.6)[51]. From the value of f=0.24, attenuation

of the first ionization chamber is set at approximately 20%. Calculation of the optimum sample thickness can proceed by use of equation 3.4.

$$\mu \simeq \frac{\rho\sigma(E_{edge})}{Mm_N} \tag{3.4}$$

where $\sigma(E_{edge})$ is the weighted average absorption cross-section at the edge energy in m^2atom^{-1}, M is the weighted average molecular mass of the sample in a.m.u., m_N the mass of a neutron in kg, and ρ the weighted average density of the sample in kgm^{-3}.

Other factors however, can affect the choice of sample thickness, notably the presence of pinhole voids within the sample (resulting in some part of the beam not being attenuated by the sample), fluorescence photons counted by the ion chamber, and harmonics present in the X-ray beam, all of which tend to reduce the apparent absorption cross-section of the sample. Most of these effects can be overcome by using sufficiently thin samples (again, from [51] $\mu t \leq 1.5$), having a small solid angle subtended by the detector, and offsetting one of the crystals in the two monochromator which can reduce the harmonics by several orders of magnitude. Transmission EXAFS is usually performed on concentrated or thick samples.

- Fluorescence. This type of EXAFS experiment takes advantage of the radiative processes of relaxation the core hole undergoes, and can be performed using

essentially the same collimating and focusing apparatus, the only major difference being the replacement of the second ion chamber with a photomultiplier tube at roughly 45° to the sample, as shown in Figure 3.5.

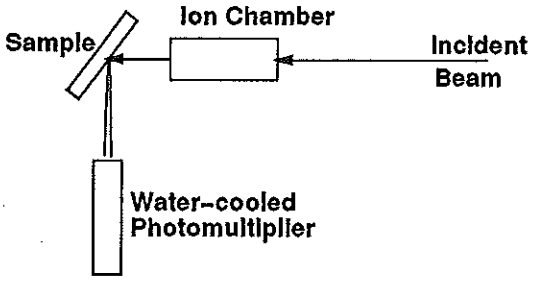

Figure 3.5: Typical Fluorescence EXAFS beamline set-up

The fluorescence yield, f, of an element, increases with atomic number Z, therefore making fluorescence experiments more viable for samples containing heavier elements. Biological compounds are often examined using Fluorescence EXAFS (FLEXAFS) as this technique is several orders of magnitude more sensitive to low concentrations of atomic species[52, 53] (compounds such as metalloproteins such as haemoglobin are an obvious example of such compounds with a heavy metal atom present in low concentrations).

Fluorescence experiments are usually performed on samples that are particularly thin, or contain very dilute species (of around 10^{16} atoms)

- Auger electron EXAFS (SEXAFS). This method of measuring the X-ray absorption coefficient of the sample measures directly the secondary electrons

produced as the core hole relaxes; Auger electrons. the Auger electron yield is complementary to the fluorescence yield, being higher for lighter elements. The primary advantage of this technique relies on the fact that electrons have a restricted penetration depth within a solid sample, and the extracted $\mu(E)$ contains information about regions close to the surface of the sample (within about 100Å), and is thus used in the study of adsorption onto surface sites (the polarization of the beam, ϵ, will be involved here as it relates to the orientation of the crystal lattice of the sample r). The nature of SEXAFS requires that electrons, not photons, are detected. For this reason the experimental arrangement here will differ significantly from transmission or fluorescence EXAFS (in particular a high vacuum is required)

Chapter 4

EXAFS Results

4.1 Calibration Samples

To obtain values for the mean free path of the photoelectron and the amplitude reduction factor due to non-EXAFS processes (denoted VPI and AFAC respectively in the EXCURV90 package) calibrants of known coordination numbers, bond lengths and chemical composition are first analysed. In this instance, foil samples are used, as coordination numbers are easy to calculate, and bond distances are tabulated in chemical catalogues (such as the CRC handbook of chemistry and physics[54]).

4.1.1 Gold Foil

Spectra of gold foil samples were taken at 80K and room temperature. Five statistically significant shells were fitted, with coordination numbers being fixed to allow VPI and AFAC to be floated. Results for the foil are shown in tables 4.1 and 4.2.

Table 4.1: EXAFS results for Au foil at 80K

R_{expt} (Å)	R_{calc} (Å)	N (atoms)	A_{80K}(Å^2)
2.85	2.85	12	0.008
4.03	4.03	6	0.012
4.95	4.93	24	0.016
5.62	5.7	12	0.008
6.35	6.37	24	0.027

Table 4.2: EXAFS results for Au foil at room temperature

R_{expt} (Å)	R_{calc} (Å)	N (atoms)	A_{rt}(Å^2)
2.83	2.83	12	0.016
4.00	4.00	6	0.024
4.89	4.90	24	0.031
5.54	5.66	12	0.022
6.29	6.32	24	0.032

As it can be safely assumed that the foils posses *no* static disorder, any resultant disorder at 80K is attributed to the Zero Point vibrational energy of the system.

Table 4.3: Disorder contributions for Au foil

Shell	σ^2_{total} x10^{-3}Å^2	σ_{rt} (Å)	σ_{80K} (Å)
1	0.008	0.089	0.063
2	0.012	0.11	0.077
3	0.015	0.12	0.089
4	0.011	0.10	0.063
5	0.016	0.13	0.12

Once bond lengths had been correctly fitted, analysis proceeded by calculating the optimum AFAC and VPI values.

Evaluation of AFAC and VPI are based on the 80K sample as the EXAFS function is less noisy, partly due to the lowering of Debye-Waller factors.

The normalised EXAFS function and Fourier transform are shown in Figures 4.1 and 4.2.

AFAC is intrinsically linked to coordination numbers and Debye-Waller factors. As the Coordination numbers are fixed for the calibrant, the correlation between AFAC and the A values (where $A=2\sigma^2$ as before), and between AFAC and VPI is examined. Iteration is used to find appropriate minimum for AFAC and VPI to be used for the clustered samples. It is assumed that these values are readily transferable between samples.

The correlation map for AFAC and VPI is shown in Figure 4.3, the minimum is at an AFAC value of 0.54, and a VPI value of -4.28. These values are used throughout the analysis of the gold clusters.

4.1.2 Palladium Foil

Spectra of the palladium foil were taken only at 80K. Results are shown in Table 4.4.

The EXAFS function and Fourier transform of the palladium foil are shown in Figures 4.5 and 4.6. Figure 4.4 shows the correlation between AFAC and VPI values.

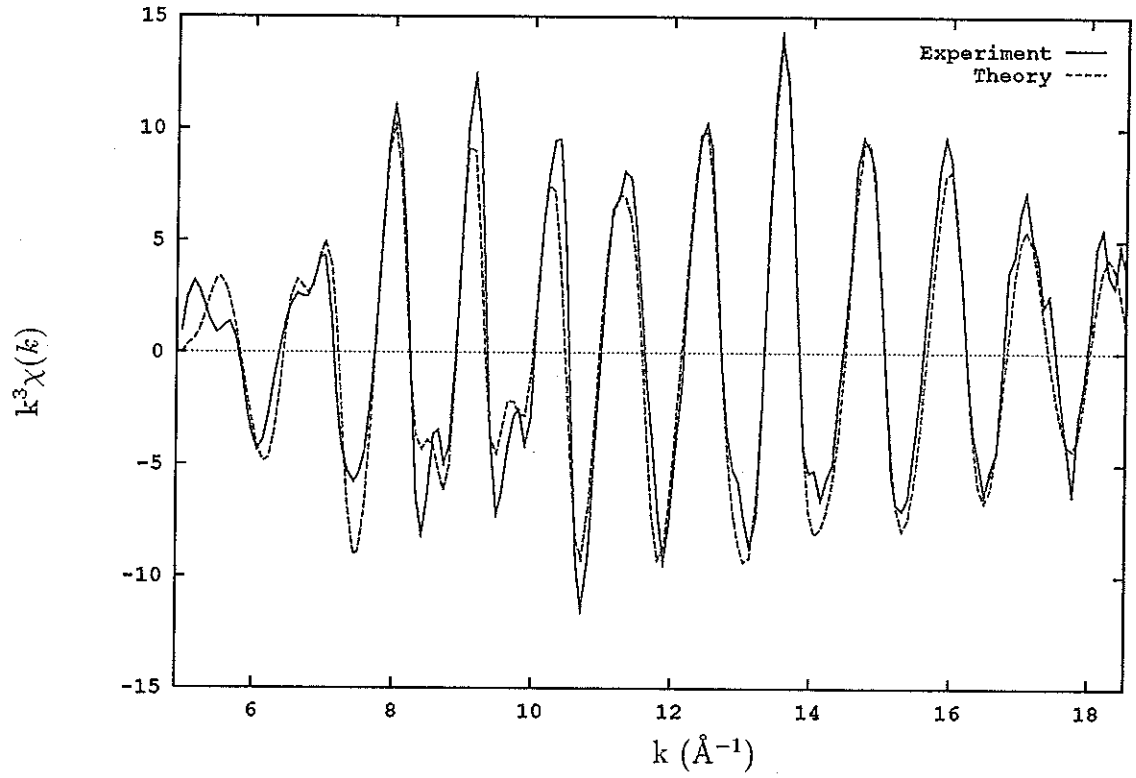

Figure 4.1: EXAFS function for gold foil at 80K

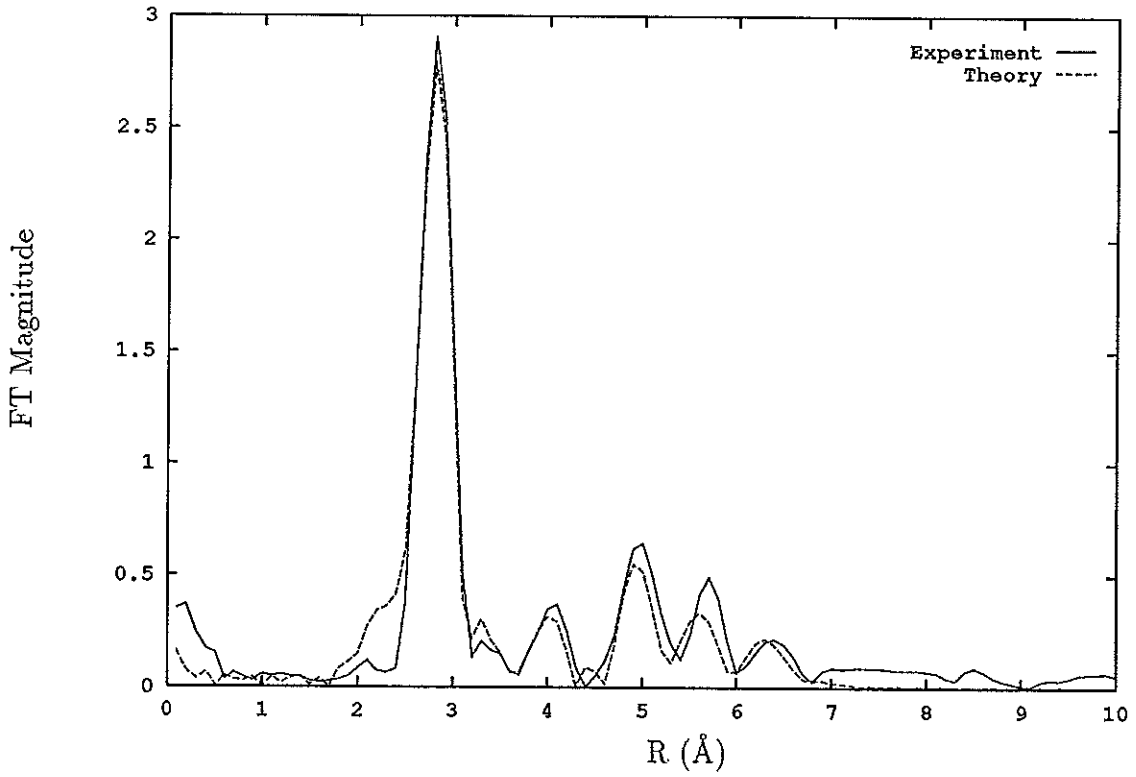

Figure 4.2: Fourier transform of gold foil EXAFS data

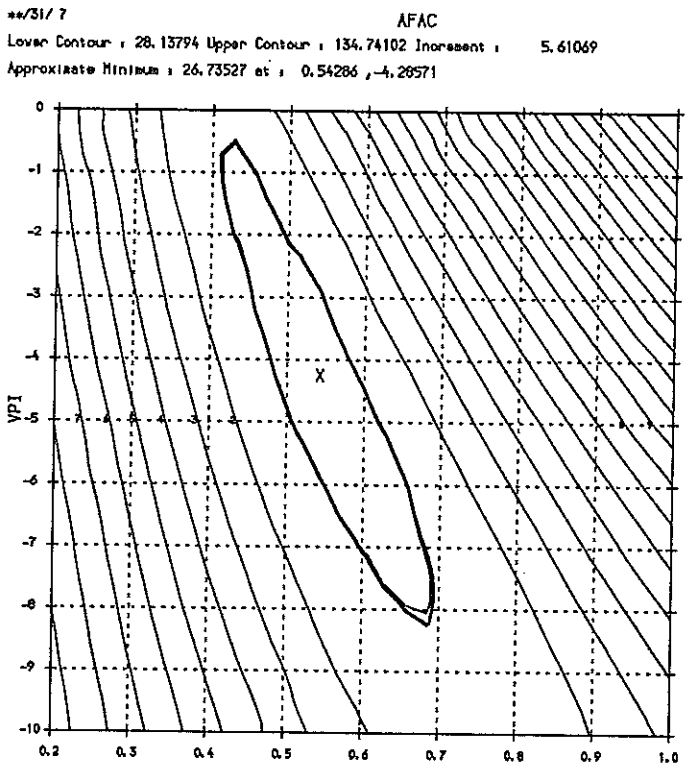

Figure 4.3: Correlation Map of AFAC and VPI for gold foil at 80K

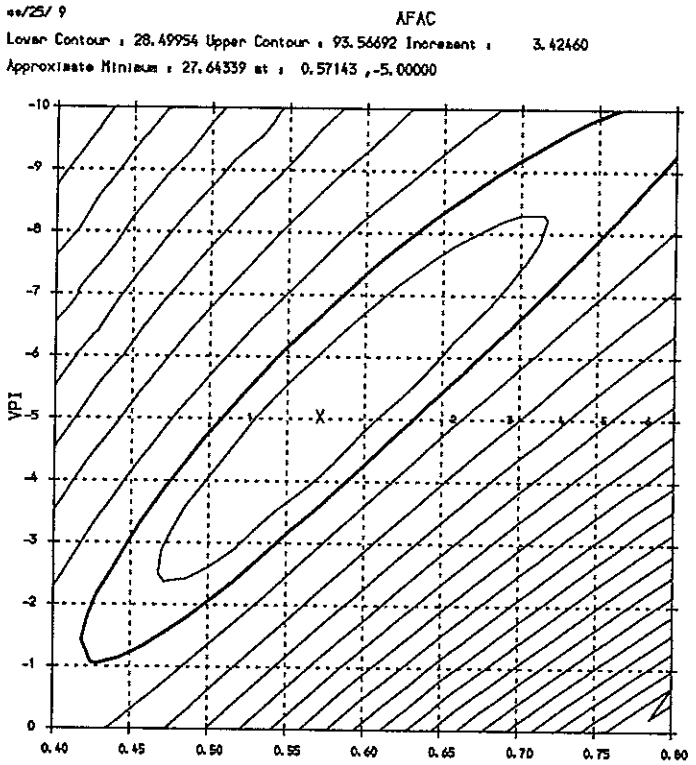

Figure 4.4: Correlation map of AFAC and VPI for Palladium foil at 80K

Table 4.4: EXAFS results for Pd foil at 80K

Shell	R_{expt} (Å)	R_{calc} (Å)	N (atoms)	A(Å^2)	σ_{80K} (Å)
1	2.73	2.73	12	0.007	0.06
2	3.86	3.86	6	0.014	0.084
3	4.73	4.73	24	0.012	0.077
4	5.46	5.46	12	0.007	0.059
5	6.11	6.11	24	0.013	0.081

An appropriate minimum was found at an AFAC value of 0.57, and VPI of -5.0.

4.2 Gold-11 Cluster

EXAFS results for this compound are summarized in Table 4.5. Because spectra were only taken at 80K, no comment regarding the change in σ^2_{rt} with respect to cluster size can be made (useful if the mobility of the surface atoms were to be investigated[16]), but σ_{80K} can be calculated, and is included in the table.

Table 4.5: EXAFS results for Au_{11} at 80K

Assigned Peak	R Å(±Å)	N atoms (± atoms)	A Å^2 (± Å^2)	σ_{80K} (Å)
Au	2.66 (0.009)	1 (2)	0.007 (0.006)	0.06
Au	2.88 (0.03)	3(2)	0.012 (0.005)	0.08
Au	4.69 (0.03)	3 (4)	0.016 (0.007)	0.09
P	2.28 (0.04)	1 (1)	0.009 (0.007)	0.06
I	2.65 (0.06)	4 (2)	0.029 (0.008)	0.12

The EXAFS function itself, together with the accompanying Fourier transform is shown in Figures 4.7 and 4.8

The correlation map plot for this sample shown in Figure 4.9 indicates the presence of a secondary peak (not visible in the Fourier transform), whilst the correlation

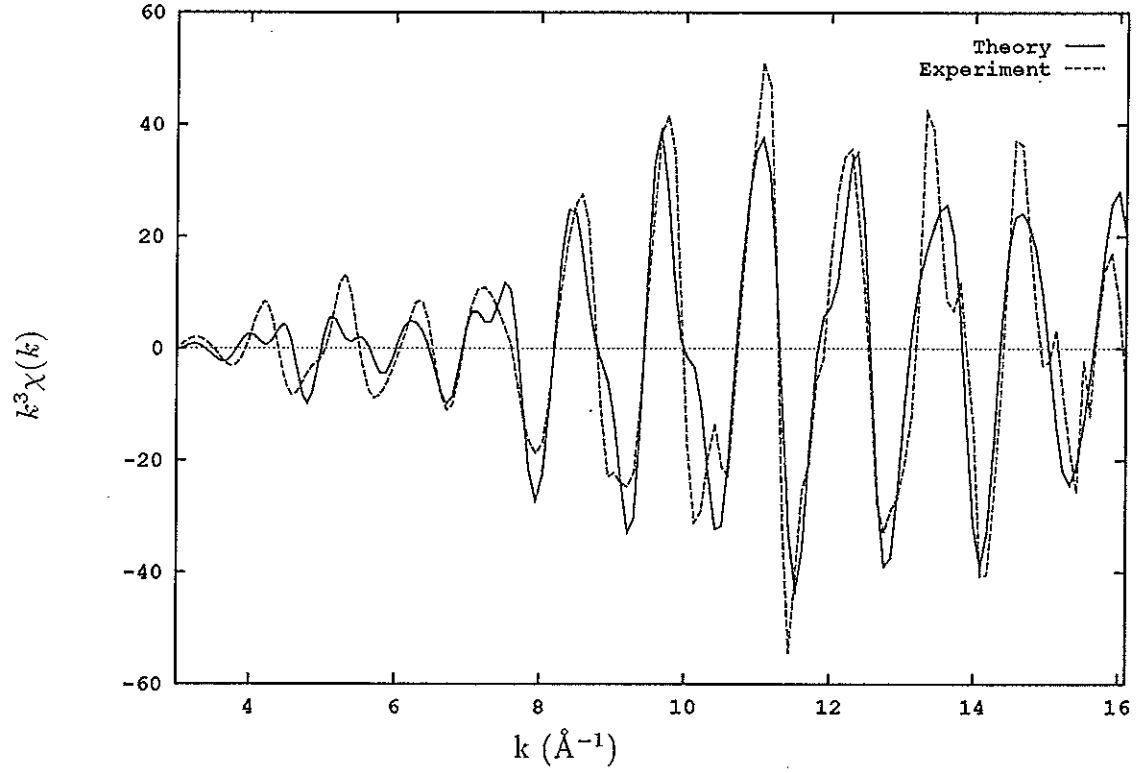

Figure 4.5: Palladium Foil EXAFS function (80K)

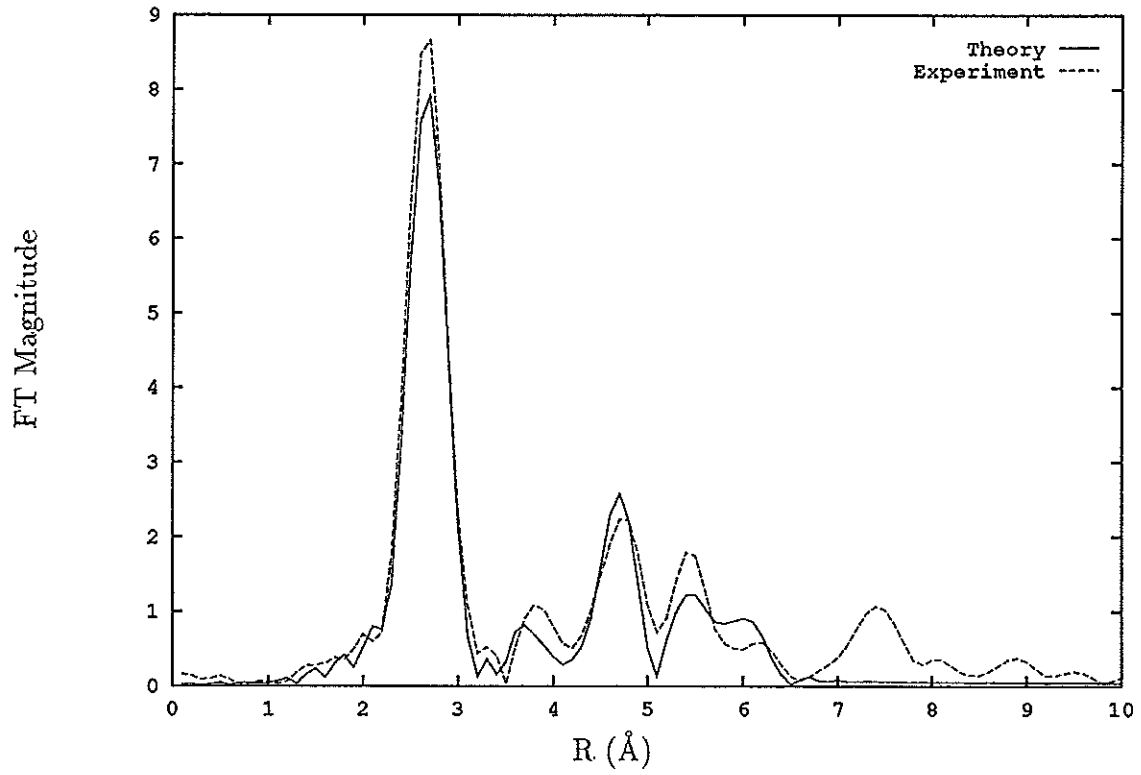

Figure 4.6: Palladium Foil Fourier Transform (80K)

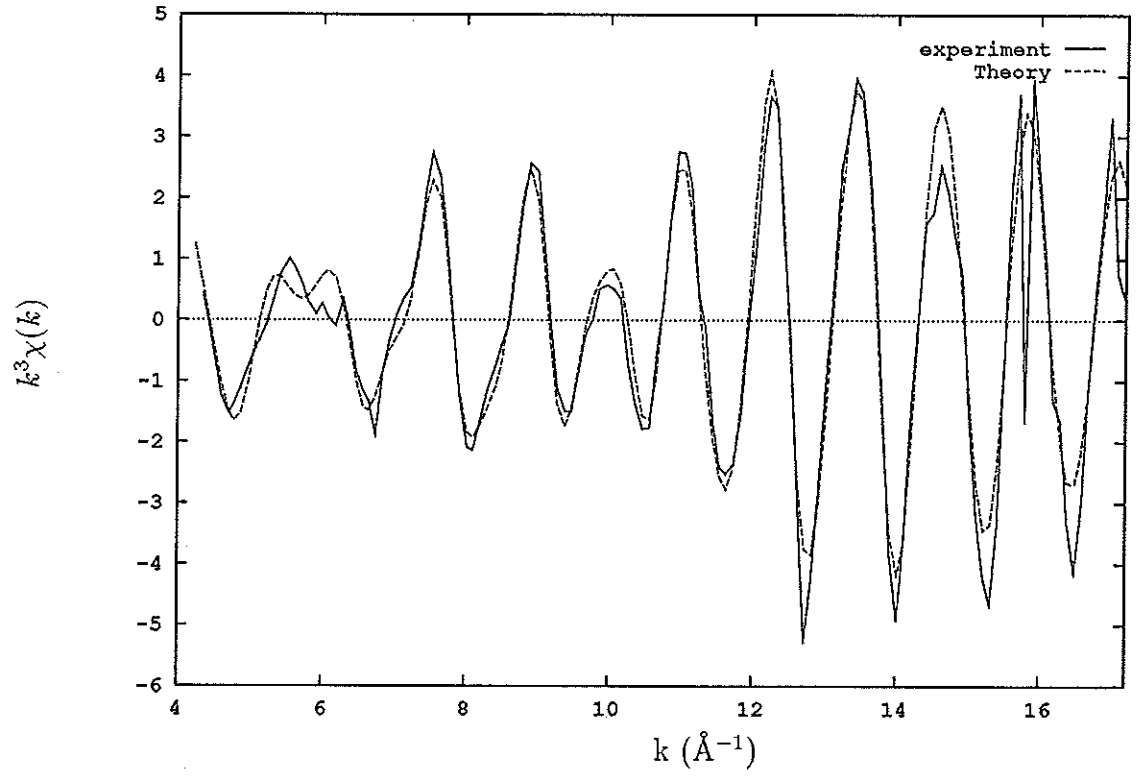

Figure 4.7: Au_{11} (80K) EXAFS Function

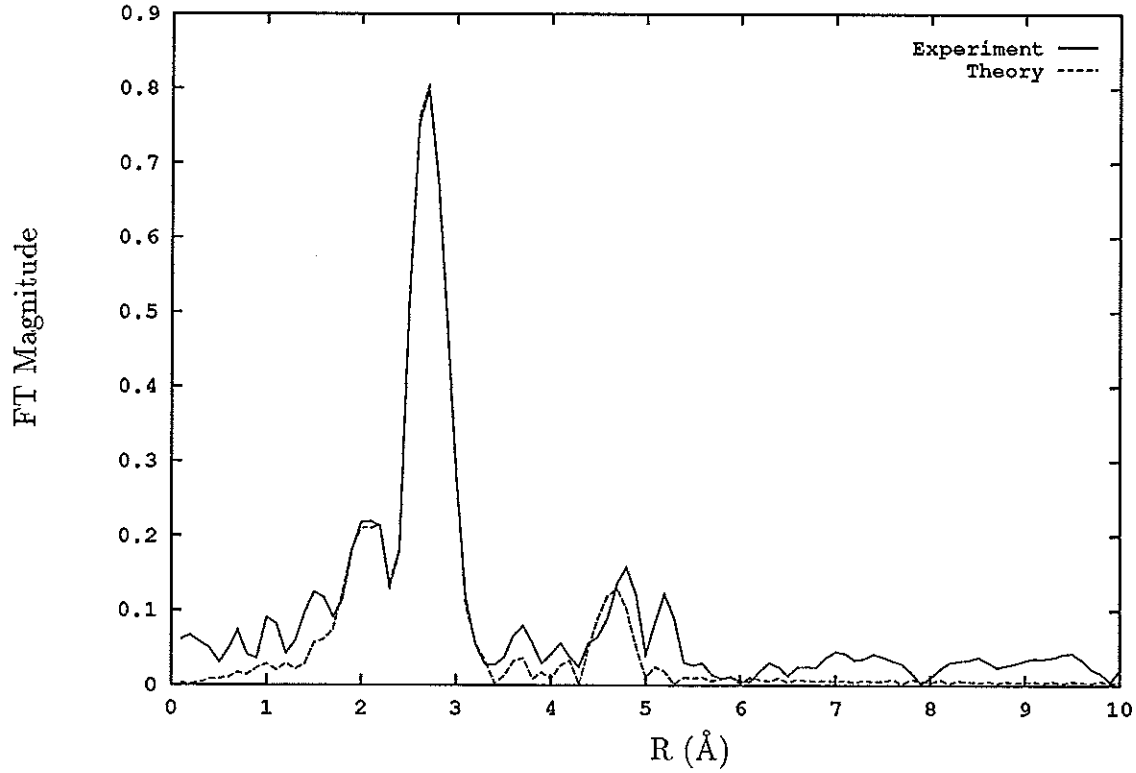

Figure 4.8: Au_{11} (80K) Fourier Transform

between A1 and N1 is shown in Figure 4.10.

The presence of the subsidiary shells consisting of Au-P and Au-I contributions is shown by the correlation map plots of R4 vs E_0 in Figure 4.11, and R5 vs E_0 in Figure 4.12

4.3 Gold-55 cluster

Results for the Au_{55} cluster are shown in table 4.6 and 4.7. EXAFS functions and Fourier transforms are shown in Figures 4.14 and 4.15.

Table 4.6: EXAFS results for Au_{55} at 80K

Assigned Peak	R Å(± Å)	N atoms (± atoms)	A_{80K} Å^2 (± Å^2)	σ_{80K} (Å)
Au	2.75 (0.004)	8 (1)	0.019 (0.001)	0.097
Au	3.93 (0.03)	5 (7)	0.042 (0.02)	0.145
Au	4.88 (0.008)	1 (0.5)	0.002 (0.005)	0.03
P	2.30 (0.017)	1 (0.3)	0.006 (0.002)	0.05
Cl	2.50 (0.008)	2 (1)	0.02 (0.008)	0.1

Room temperature EXAFS function and Fourier transform is illustrated in Figures 4.16 and 4.17

Table 4.7: EXAFS results for Au_{55} at room temperature

Assigned Peak	R Å(± Å)	N atoms (± atoms)	A_{rt} Å^2 (± Å^2)	σ_{rt} (Å)
Au	2.72 (0.01)	6 (1)	0.021 (0.002)	0.10

The correlation map plots (Figure 4.18) show the localisation of the primary minimum (i.e. R1), and show no signs of a split first near neighbour peak.

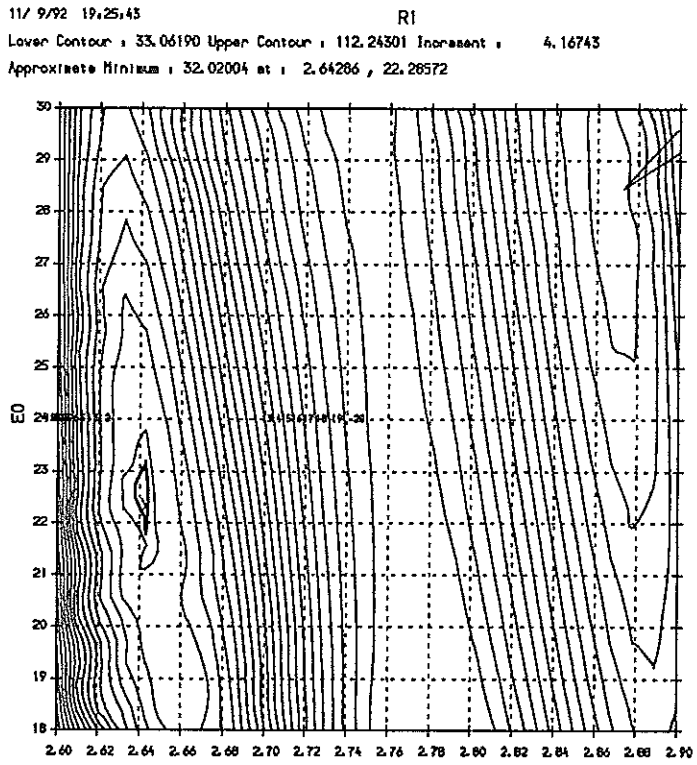

Figure 4.9: Au_{11} correlation map plot for first coordination shell

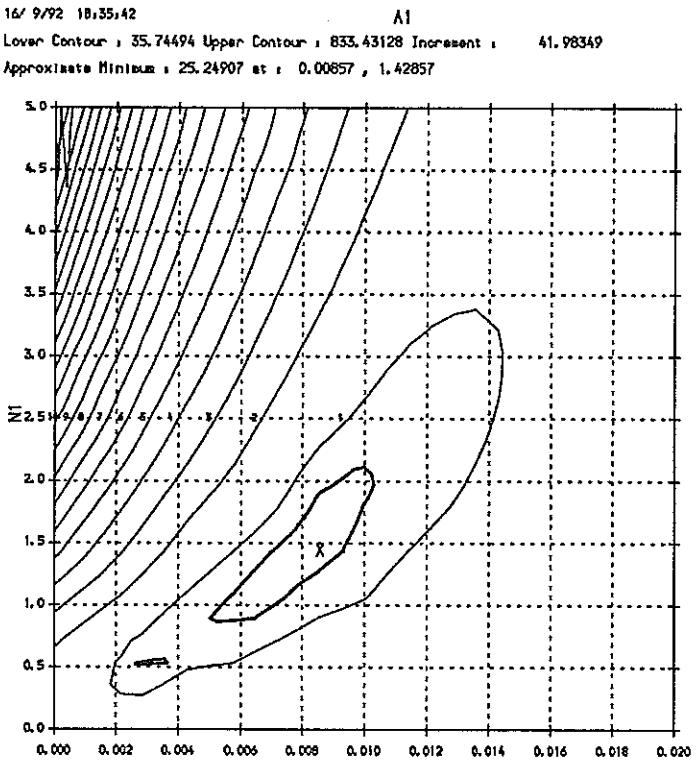

Figure 4.10: A1 vs N1 correlation map for Au_{11}

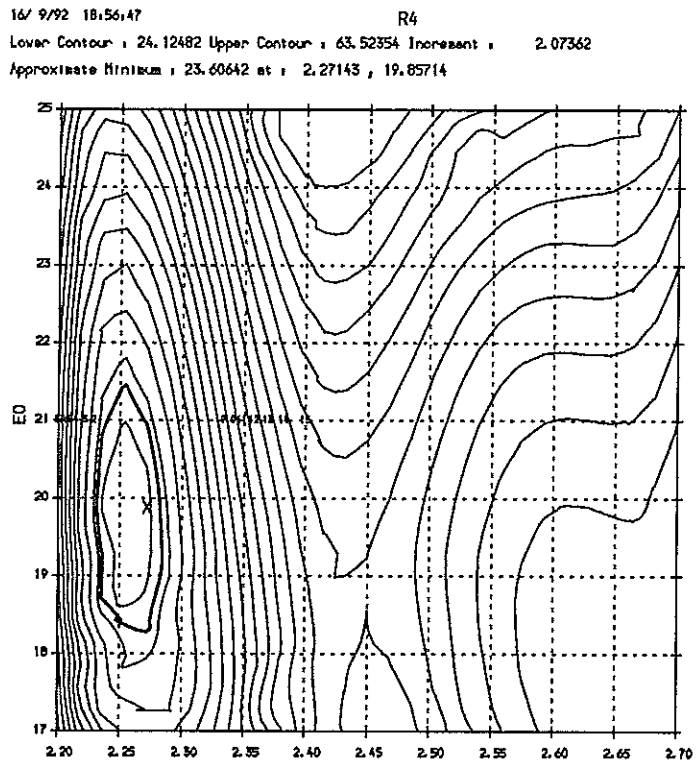

Figure 4.11: R4 vs E_0 for Au_{11} showing presence of P sub-shell

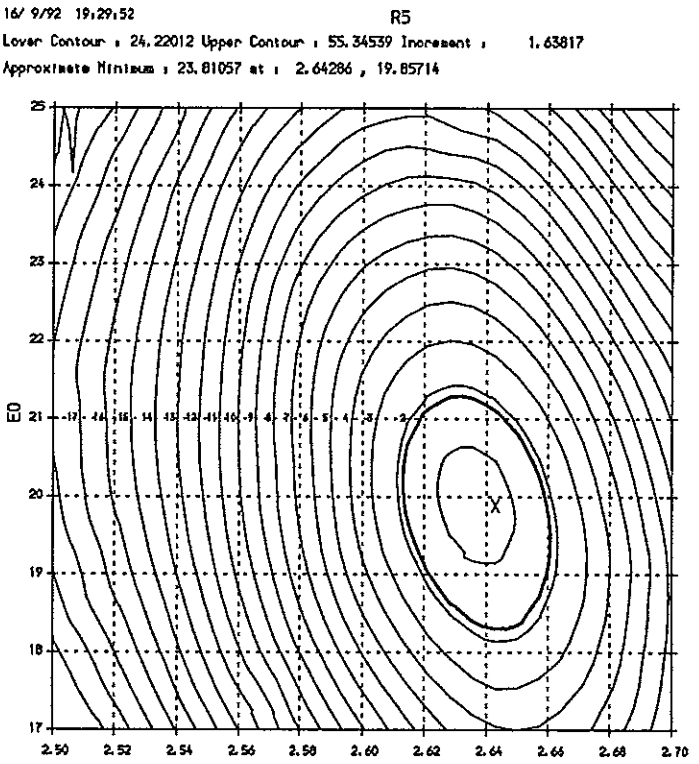

Figure 4.12: R5 vs E_0 for Au_{11} showing presence of I sub-shell

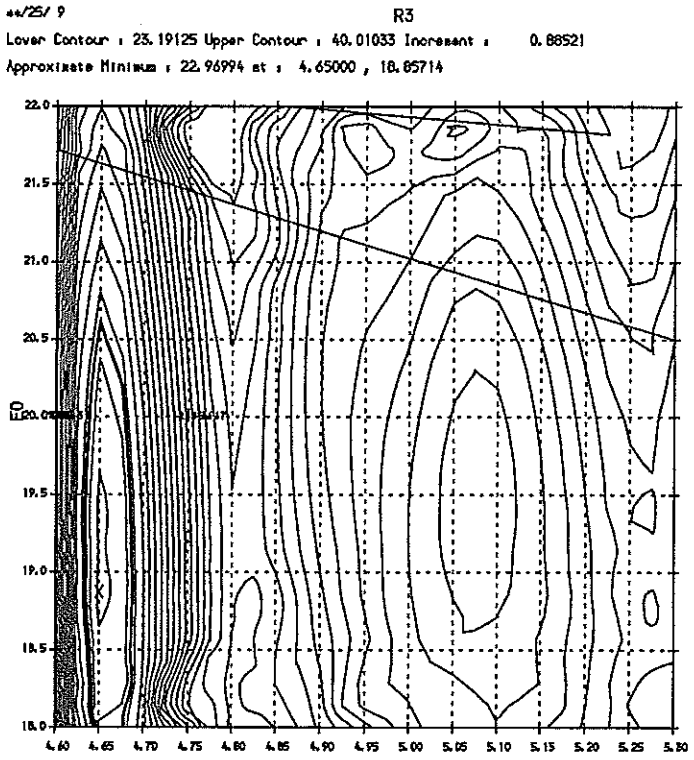

Figure 4.13: Additional (unfitted) Au-Au coordination shell of Au_{11}

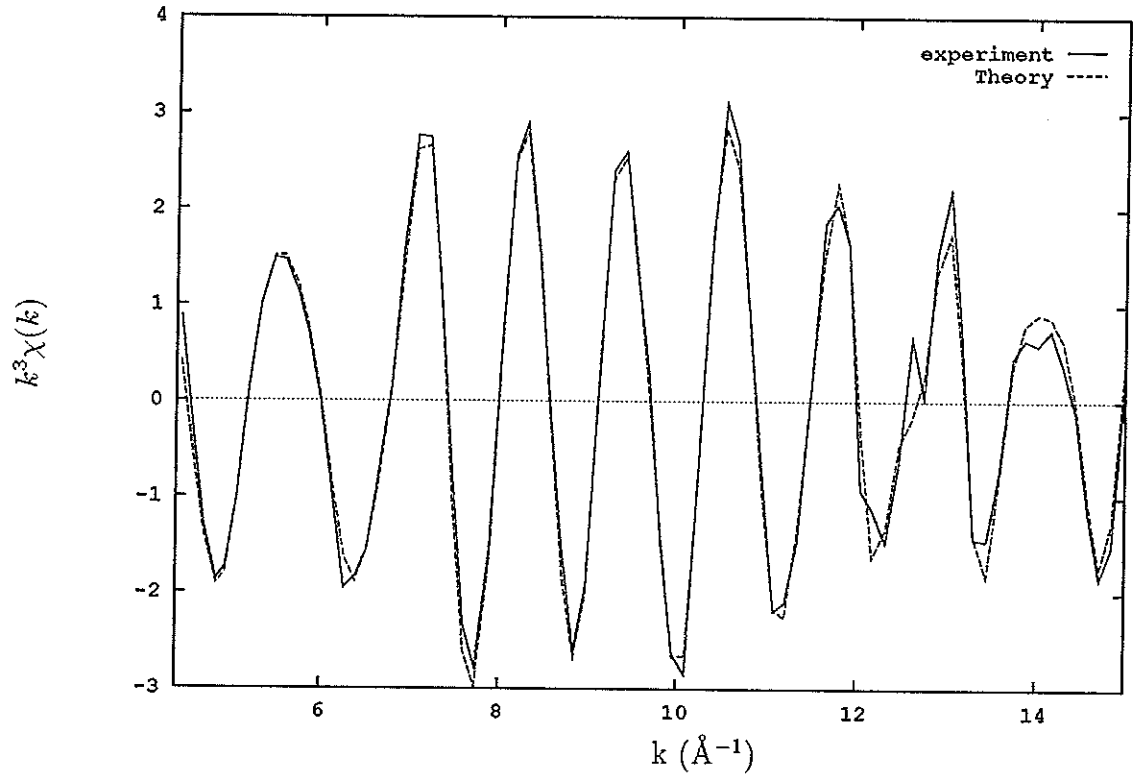

Figure 4.14: Au_{55} at 80K EXAFS function

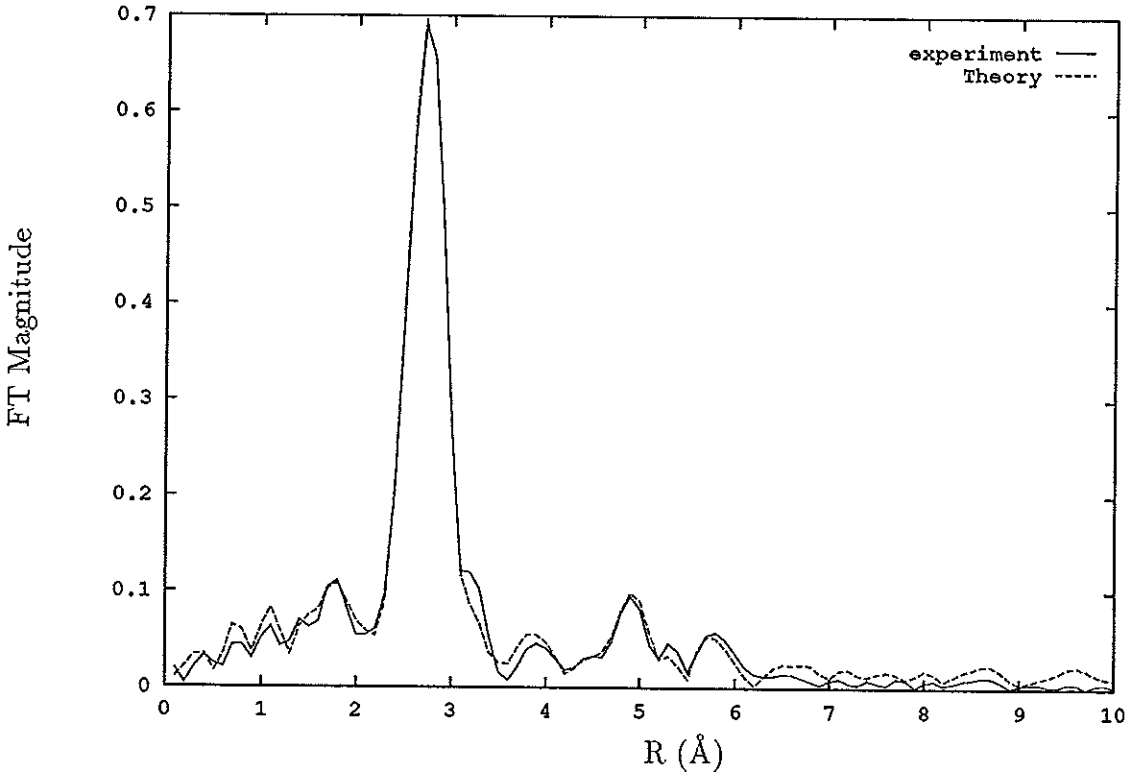

Figure 4.15: Au_{55} at 80K, Fourier transform

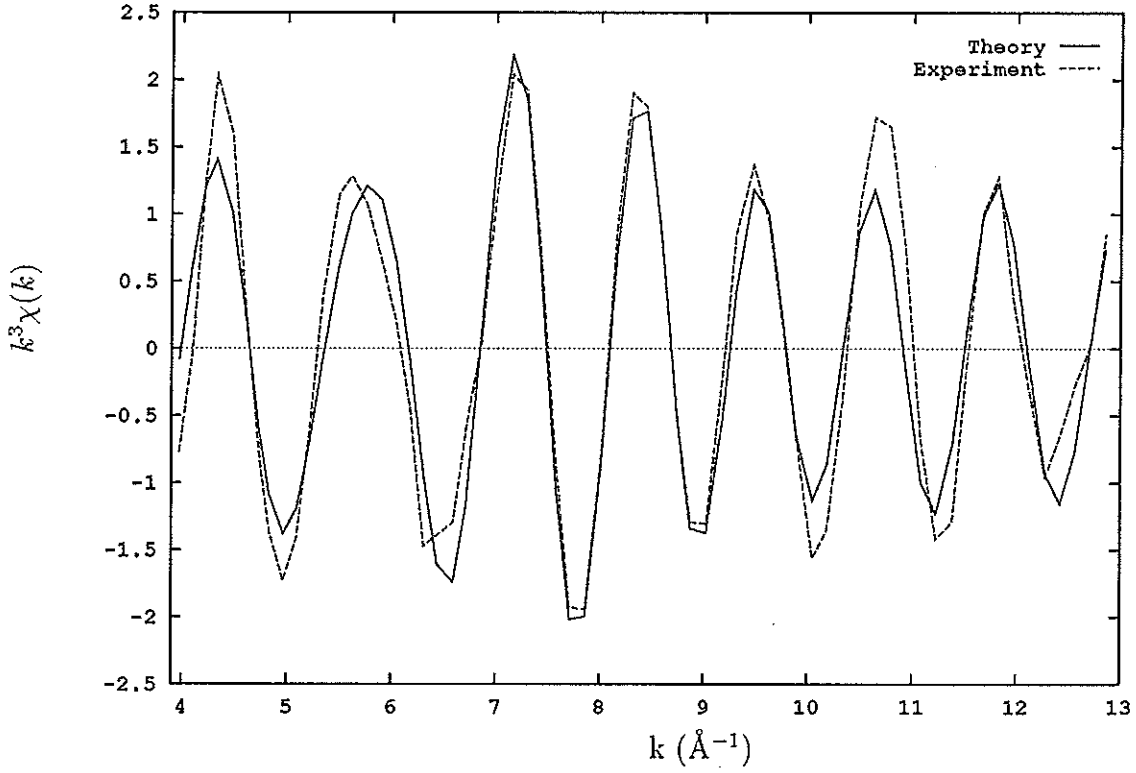

Figure 4.16: Au_{55} at room temperature, EXAFS function

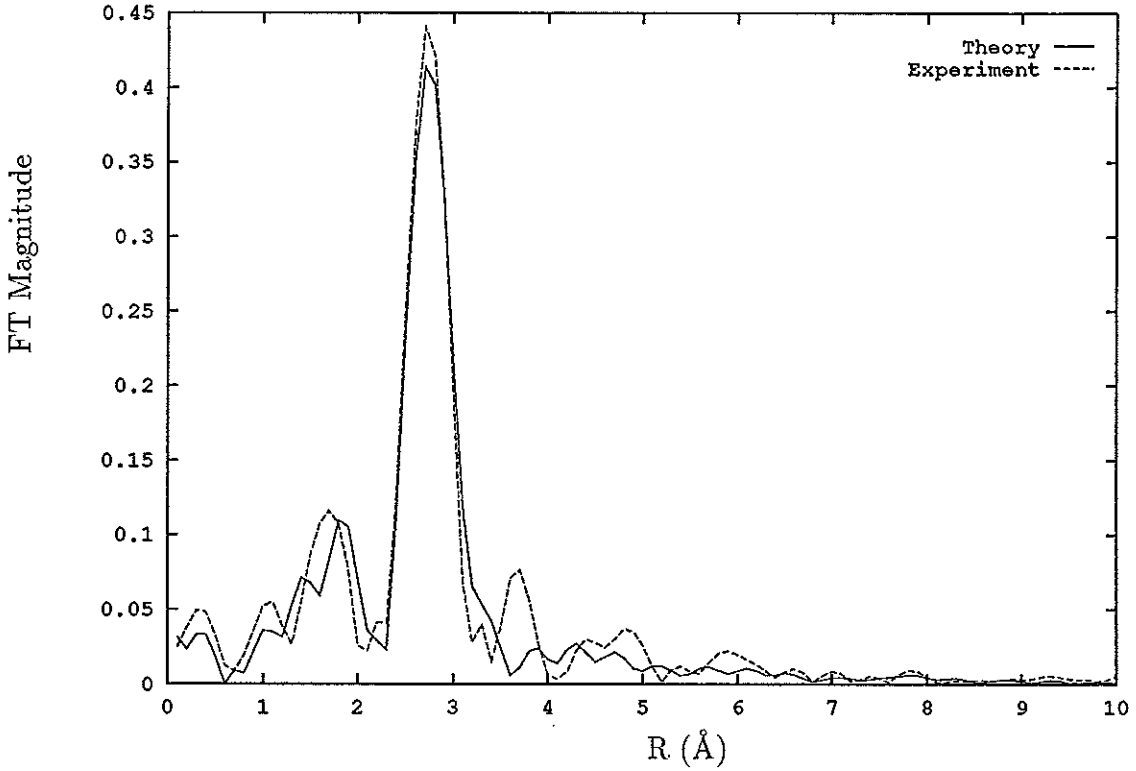

Figure 4.17: Au_{55} at room temperature Fourier transform

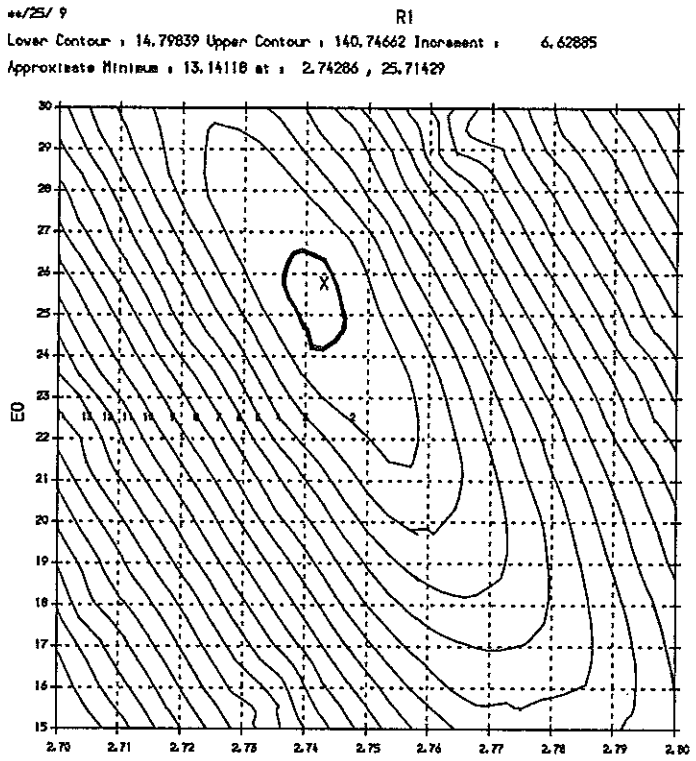

Figure 4.18: Au_{55} correlation map plot of R1 vs E_0

Further correlation plots are shown in Figures 4.19-4.21, showing correlation between separate shells.

Soluble gold-55 cluster

As results indicate that no dramatic structural rearrangement has occurred during sulphonation of the cluster, results for the soluble cluster will be given here also.

Table 4.8: EXAFS results for Au^{*}_{55} at 80K

Assigned Peak	R Å(±Å)	N atoms (± atoms)	A Å^2 (± Å^2)
Au	2.79 (0.006)	6 (1)	0.017 (0.001)
Au	3.97 (0.03)	4 (5)	0.032 (0.02)
Au	4.9 (0.02)	1 (2)	0.13 (0.01)
P	2.27 (0.02)	1 (1)	0.017 (0.008)
Cl	2.47 (0.02)	5 (3)	0.55 (0.02)

4.4 Giant Palladium Cluster

The much larger proportion of metal atoms compared to ligands in this cluster prevents any definitive statements concerning the nature of the ligands present, however, four statistically significant coordination shells of palladium have been fitted to the EXAFS spectrum obtained. Results are summarized in table 4.9. The EXAFS function and Fourier transform of these data are shown in Figures 4.24 and 4.25 respectively.

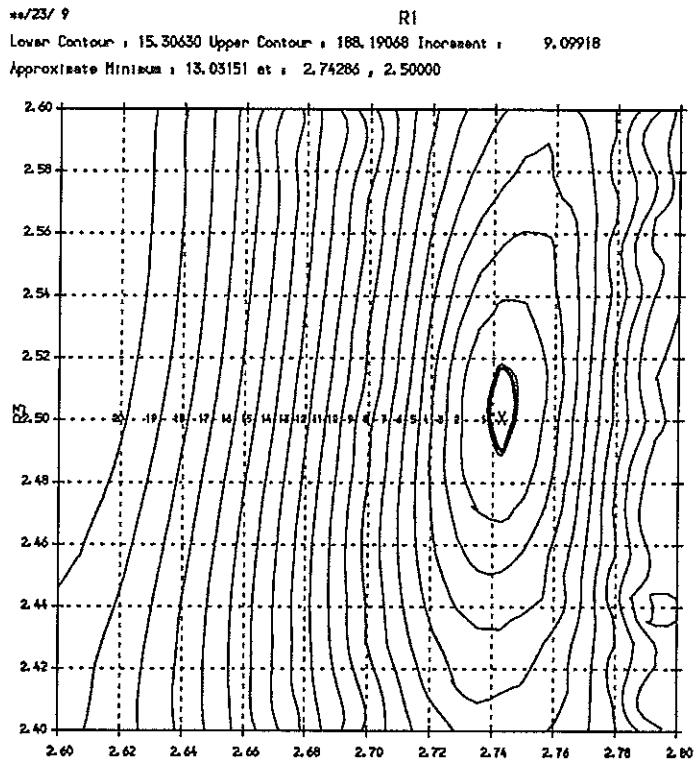

Figure 4.19: Correlation between primary gold peak and chlorine shell for Au_{55}

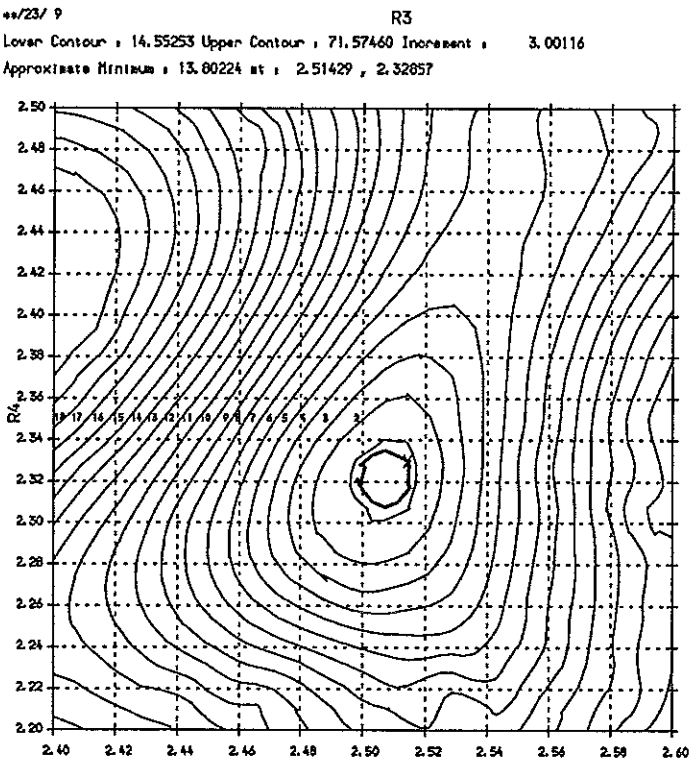

Figure 4.20: Correlation between phosphorus and chlorine bond distances for Au_{55}

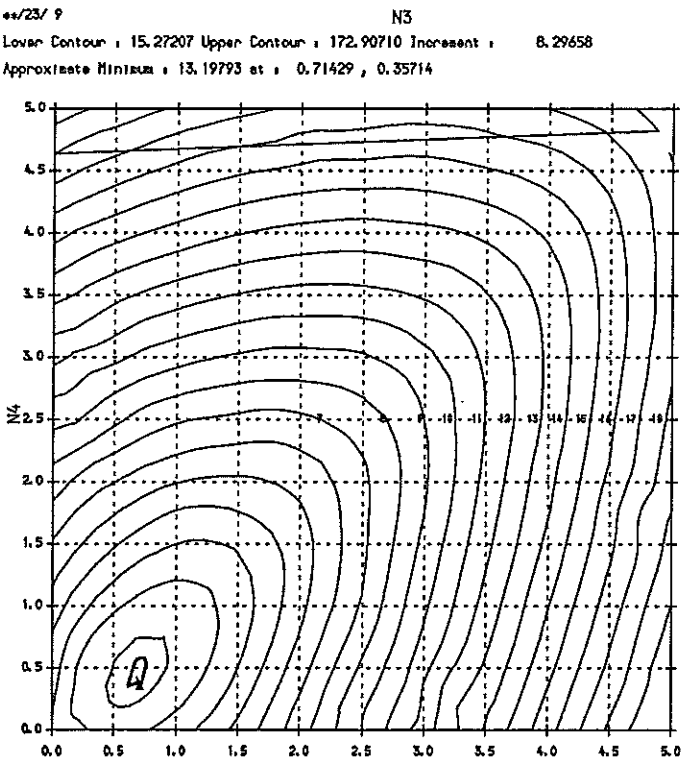

Figure 4.21: Correlation between phosphorus and chlorine coordination numbers for Au_{55}

Table 4.9: EXAFS results for Pd_{561} at 80K

Assigned Peak	R Å(± Å)	N atoms (± atoms)	A $Å^2$(± $Å^2$)
Pd	2.74 (0.006)	6 (1)	0.007 (0.001)
Pd	3.83 (0.04)	3 (5)	0.014 (0.02)
Pd	4.75 (0.02)	3 (4)	0.005 (0.008)
Pd	5.37 (0.02)	2 (3)	0.001 (0.01)

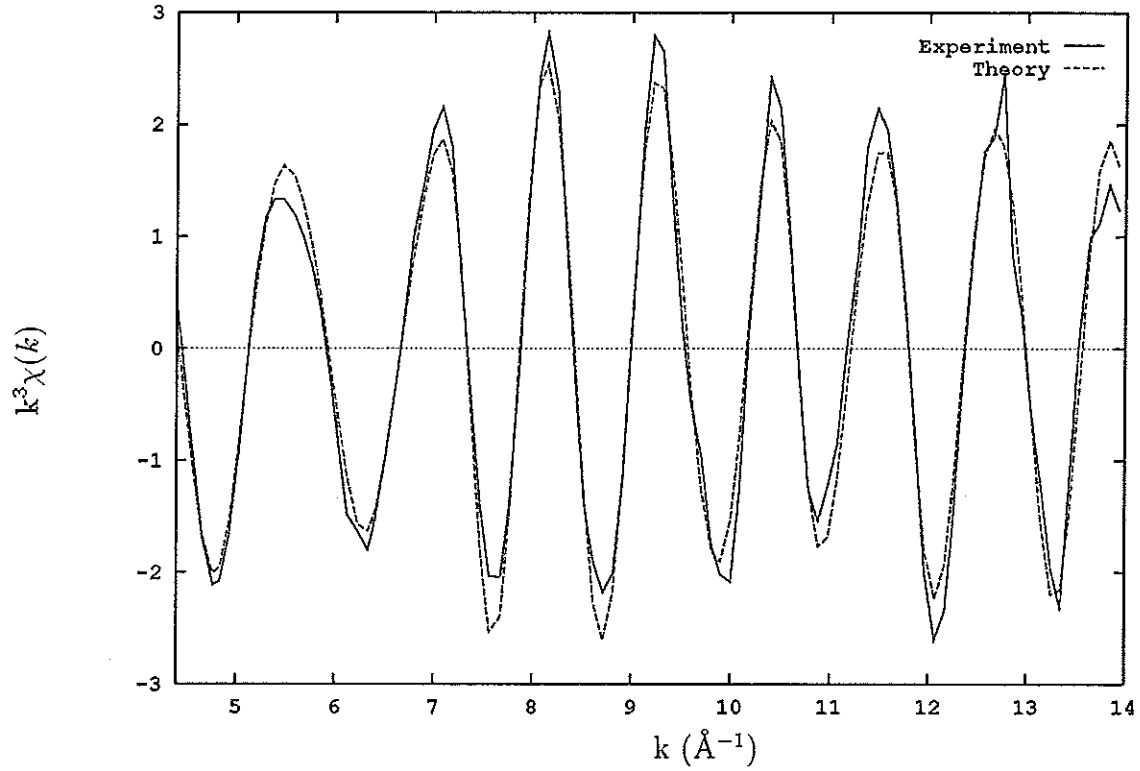

Figure 4.22: Au_{55}^* EXAFS function

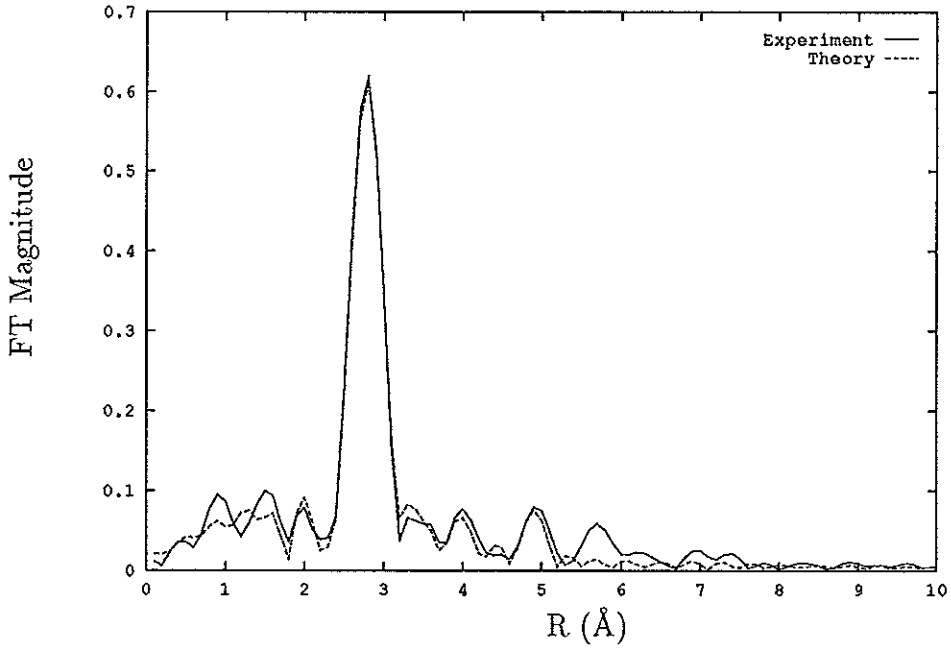

Figure 4.23: Au_{55}^* Fourier transform

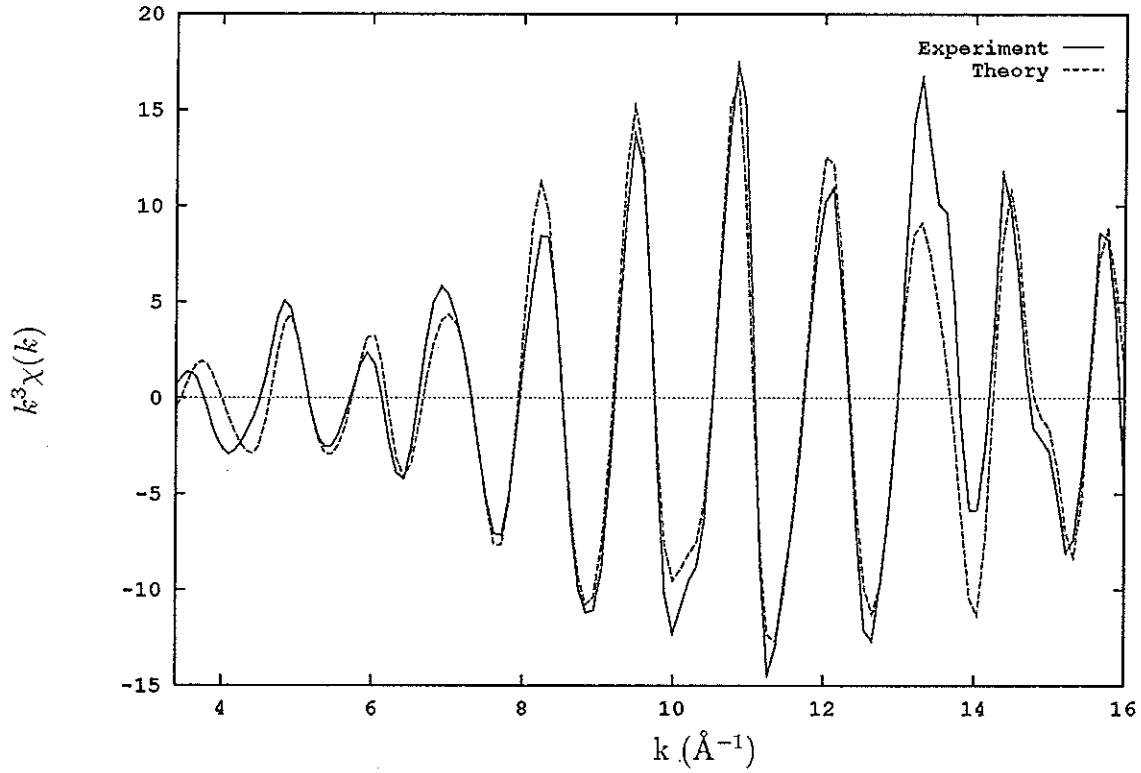

Figure 4.24: EXAFS function for Pd_{561} at 80K

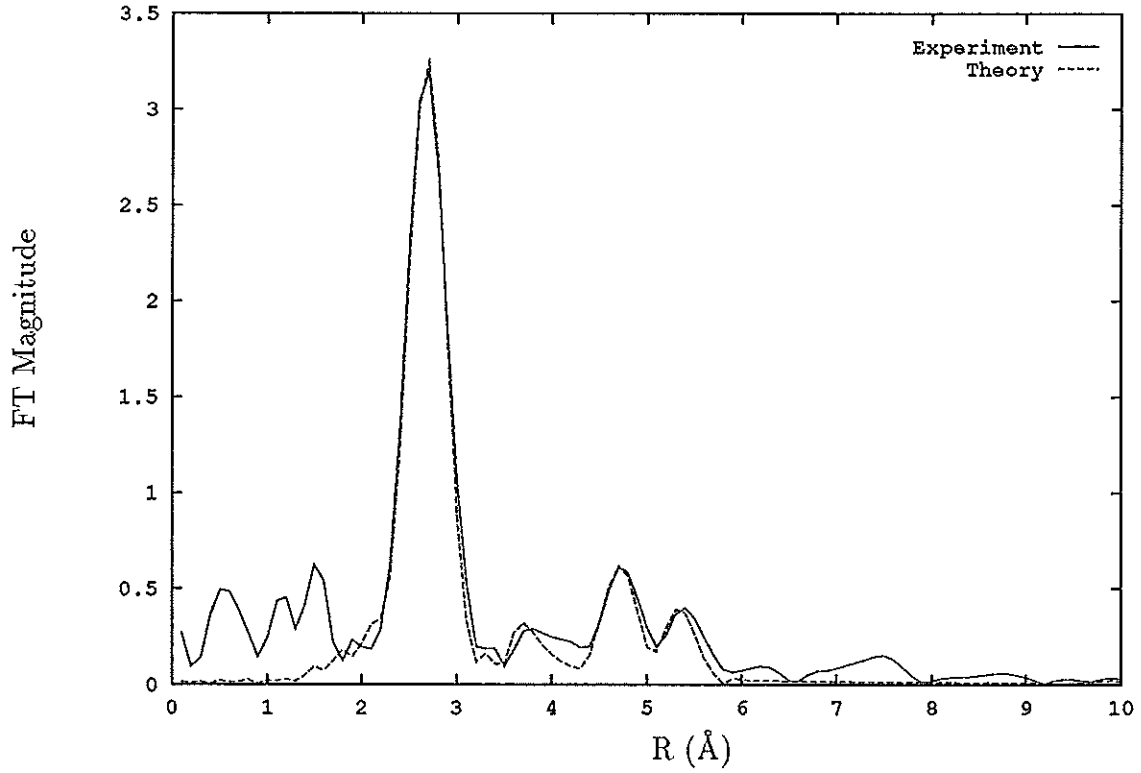

Figure 4.25: Fourier transform of Pd_{561} EXAFS data

Chapter 5

Additional Samples

In addition to the data taken for the clustered samples, EXAFS spectra have been taken for two other samples, namely:-

(a) Colloidal Gold.

(b) Purple of Cassius.

Whilst the analysis of these samples does not form a major part of this thesis, it is useful to consider them here, as they serve as examples of the wider uses of the EXAFS technique. The data shown were taken at 80K.

Colloidal Gold

Plots of EXAFS function and Fourier transform of the colloidal gold sample are shown in Figures 5.1 and 5.2.

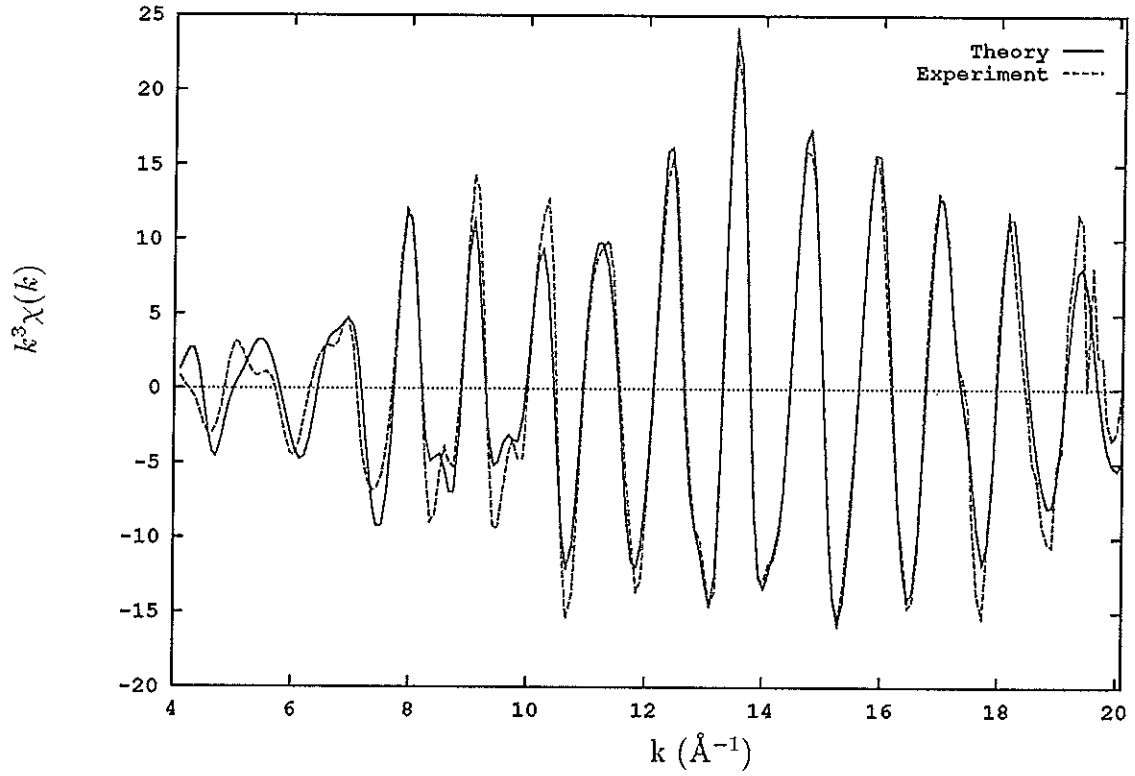

Figure 5.1: Gold Colloid in polymer, EXAFS Function.

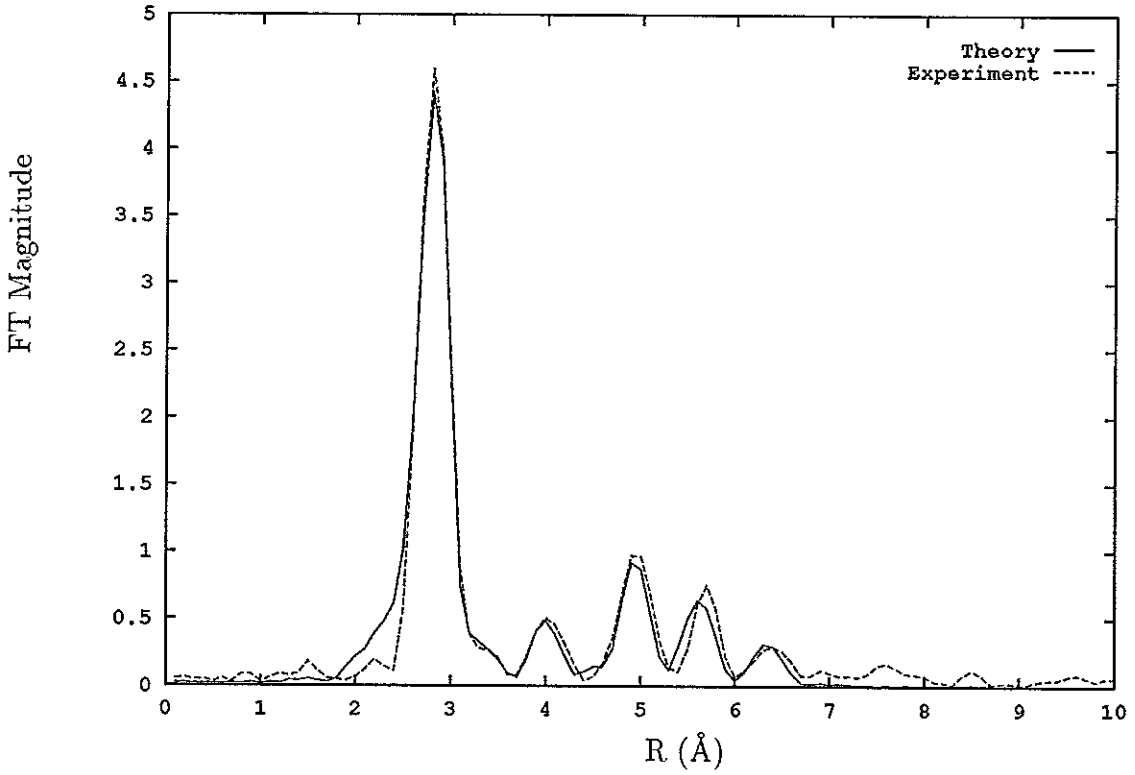

Figure 5.2: Gold Colloid in polymer, Fourier Transform.

The bond length distribution, as shown in Table 5.1, showns that the bond distances are very close to that of a close packed system (calculations based on FCC ratios, using experimental near neighbour distance as a_0) .

Table 5.1: EXAFS results for colloidal sample

R_{expt} Å(± Å)	R_{FCC} (Å)	N atoms (± atoms)	A_{80K} Å^2 (± Å^2)
2.86 (0.002)	2.86	11 (1)	0.008 (0.0004)
4.05 (0.01)	4.04	4 (3)	0.01 (0.002)
4.96 (0.008)	4.95	15 (5)	0.01 (0.002)
5.65 (0.01)	5.72	15 (8)	0.01 (0.003)

To highlight the close-packed nature of the core compared to that of metallic gold, the Fourier transforms of bulk gold and colloidal gold are overlayed on the same axes in Figure 5.3. It it clear that, like the Au_{55} sample, both samples possess similar bond length distributions, in addition to comparable coordination numbers, showing that the colloid exists as tiny fragments of bulk gold. Furthermore, as the near-neighbour distances for both samples shows little or no bond length contraction (and the mean coordination is distinctly larger than for Au_{55}), it can be concluded that the particle sizes are much larger than for the clusters.

Purple of Cassius

This interesting form of colloidal gold has been used for centuries, having been discovered in 1663 by Dr.A.Cassius in Leyden. The compound is produced when a solution of gold(III) chloride is added to tin(II) chloride, producing a purple-red colouration in the resultant mixture. The reason for the interest in Purple of Cassius is that

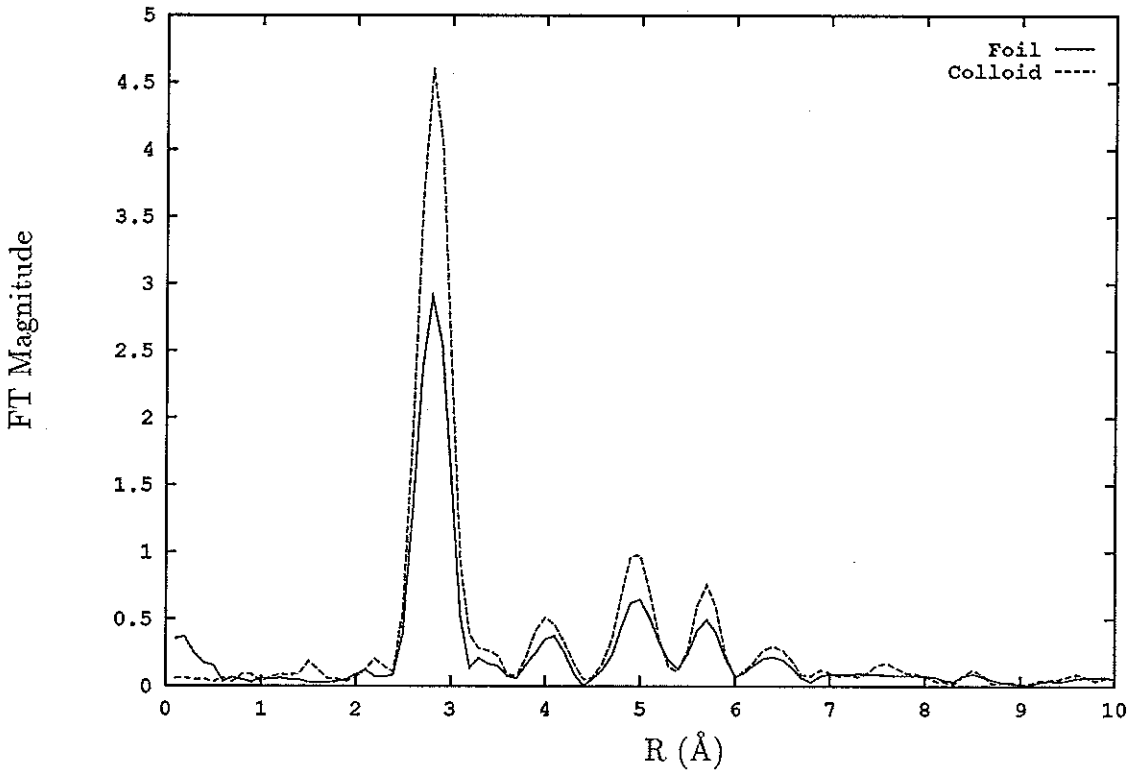

Figure 5.3: Comparison of Fourier transforms of bulk gold and colloidal sample.

there was initially some confusion as to the exact nature of the compound. It is now accepted that purple of Cassius consists of finely dispersed metallic gold particles adsorbed onto the surface of tin oxide [55]. With this in mind, EXAFS could provide a means of examining the Au-Sn bonding present.

Table 5.2, as with the other colloidal sample, highlights the similar bonding distribution pattern present (R_{FCC} distances are calculated from the first experimental bond distance as for the previous colloidal sample using a_0,$\sqrt{2}a_0$, etc).

Table 5.2: EXAFS results for purple of Cassius sample

R_{expt} Å(± Å)	R_{FCC} (Å)	N atoms (± atoms)	A_{80K} Å^2 (± Å^2)
2.86 (0.003)	2.86	11 (1)	0.008 (0.003)
4.06 (0.006)	4.04	1 (1)	0.001 (0.002)
4.96 (0.007)	4.95	9 (4)	0.007 (0.002)
5.61 (0.02)	5.7	27 (20)	0.02 (0.006)

In addition to the shells tabulated, a further coordination shell at 2.6Å was seen, and initially attributed to chlorine. Time did not allow further refinement of this peak however, so it will not be considered in detail. A correlation plot showing the existence of this peak is given for completeness in Figure 5.4.

The EXAFS function and Fourier transform for this sample are shown in Figures 5.5 and 5.6.

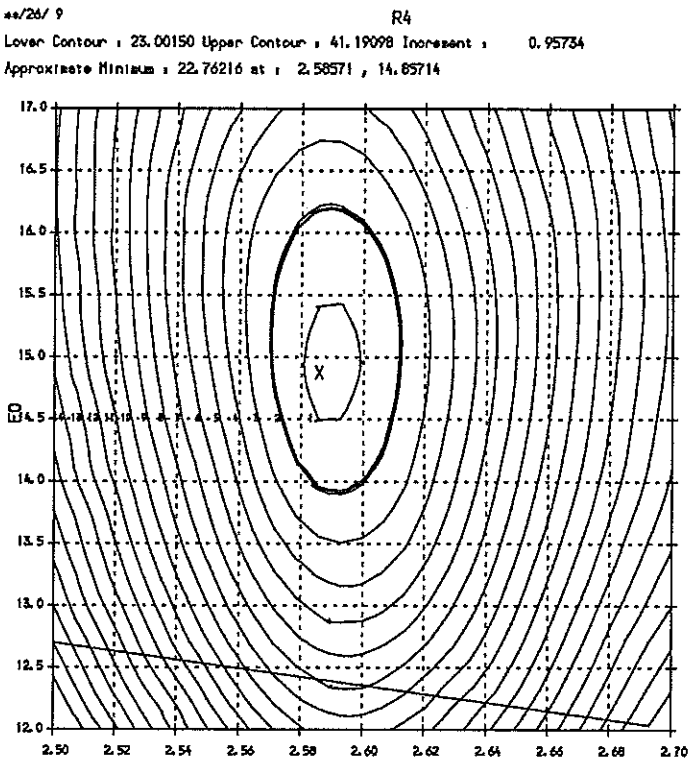

Figure 5.4: Additional coordination shell present in purple of Cassius

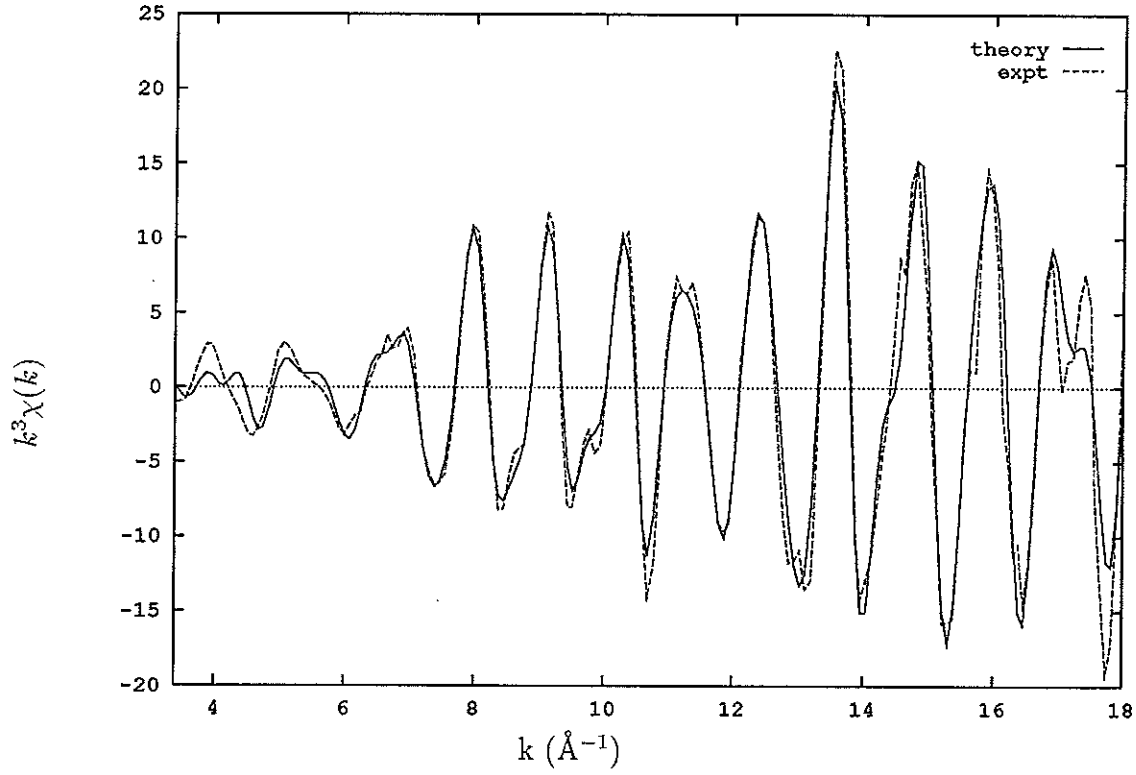

Figure 5.5: EXAFS function for Purple of Cassius

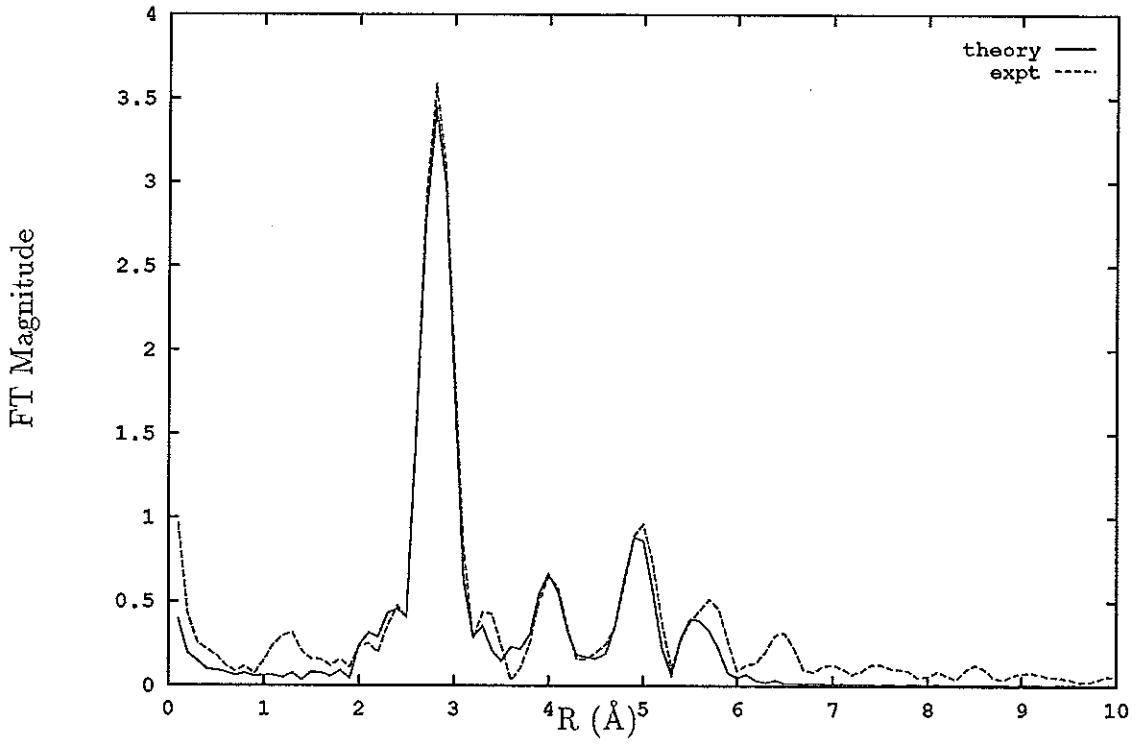

Figure 5.6: Fourier transform of Purple of Cassius

Chapter 6

Reverse Monte-Carlo Modelling

6.1 Theory

The RMC method allows one to generate a series of viable atomic configurations on the basis of experimental data[56]. Although the RMC software used here is specifically designed for use with EXAFS data and EXCURV90, the program works in essentially the same as when more commonly used for neutron or X-ray diffraction data, and the algorithm is based on the inversion of k-space data using the Metropolis Monte-Carlo method:

1. A starting configuration of the system under study is created in the form of a box of particles, usually at random positions and with suitable diameters, number density, etc. Standard Metropolis boundary conditions are then applied, i.e.

the configuration is surrounded by images of itself on all sides of the box.

2. A random particle move is then generated

3. A model EXAFS spectrum, χ_{RMC}(k) is calculated from this box and compared with the experimental χ_{expt}(k) using a reduced X^2 as a suitably weighted difference between the two spectra, where :

$$X^2 = \sum_{k=1}^{N} [\chi_{RMC}(k) - \chi_{expt}(k)]/\sigma^2 \tag{6.1}$$

If at this point X^2 has reached a sufficiently low value, indicating agreement to within the errors associated with the experimental data, then this configuration will be accepted as a viable model for the system (i.e. one in which the particle positions are consistent with the data). It is usual to continue the process and thereby generate an ensemble average.

4. If X^2 is not low enough then a particle will again be chosen at random and moved some distance in a random direction. Now a new χ_{RMC}(k) can be calculated and compared with the experimental χ_e(k) as in (1). If X^2 increases, the move is rejected subject to a probability function dependent on experimental errors; this avoids the problem of subsidiary minima. Steps (3) and (4) are repeated until convergence is achieved.

6.2 Discussion

One of the primary advantages of modelling data in this way, as opposed to the more standard approach (that of developing a theoretical model and attempting to fit it with the data obtained, as with EXCURV90), is that no assumption is made regarding the nature of the data, or the way in which they are measured. In this case no assumption is made as to the distribution of the atomic centres, something which most of the EXAFS theories discussed earlier assume that the distribution of the atomic centres about the mean bond distance are essentially Gaussian in nature, leading to the standard Debye-Waller term $e^{-2\sigma_i^2 k^2}$. This is also the drawback of modelling techniques of this type, as it does not take into account the physical/chemical rules which govern the structure of systems.

Two main problems arise from using the RMC technique with EXAFS data, both of which arise from the essentially different nature of the data between the two techniques.

To begin with, RMC assumes that the data present contains some long range information, as the Metropolis boundary conditions create an infinite array of atoms over which to carry out the calculations for the radial distribution function. EXAFS is a short range phenomenon, and its data reflects that - giving information only to about 5Å . The second problem experienced here is also connected with the information content of the data. The EXAFS function contains within it information concerning

all atom types bonded to the core excited atom. The resulting modified Fourier transform thus gives a form of *total* pair distribution function ($\rho(r)$). When modelling the 55 atom gold cluster, we are concerned only with the metal atoms present, but the EXAFS function also contains contributions from the chlorine and phosphorus shells, albeit contributions of a much lower intensity than those due to the gold-gold interactions. With this in mind, a fit from the total EXAFS function should not be considered as entirely valid.

One way to circumvent this problem is to use Fourier filtering to remove the contributions from the ligand shells, and allow RMC to fit to this data, although as already mentioned (see Analysis chapter) a consequence of Fourier filtering data, is that the information content is reduced. This method will also only be of use if the contributions from the ligand shells are sufficiently different in distance that they can be discerned on the Fourier transform. This is not the case here, as both ligand shells for the two clusters lie under the main Fourier peak of the near-neighbour gold distance.

The other option available is highly impracticable without considerable time and computing power: fitting to all atom types - a procedure which would greatly complicate the modelling process, as too many possible configurations would arise, thus slowing it down.

6.3 Results

See Figures on next page.

6.4 Conclusion

Initial work with RMC did give a reasonable fit to the EXAFS function, when the starting configuration was a cuboctahedron, and was seen to be stable, i.e. atoms did not float free of the cluster during the modelling process. However the version of RMC used needs coordination constraints to be included in the process, and even though these constraints are given a low weighting it is likely that a cluster will remain stable on the basis of the constraints alone, regardless of the data used.

The stability of the icosahedral closed shell model vs. the cuboctahdral configuration was briefly investigated. The icosahedral model was found to be less stable, i.e. for an identical number of iterations and equivalent constraints, atoms tended to float free of the starting cluster configuration during the modelling. This however, presents only tentative evidence of the true cluster geometry, and conclusions in this thesis will not rely on the modest results seen here. The advantage of RMC over other methods of analysis occurs when several sets of different experimental results are combined, as this will narrow down the number of possible structures which give a good correlation with the data used.

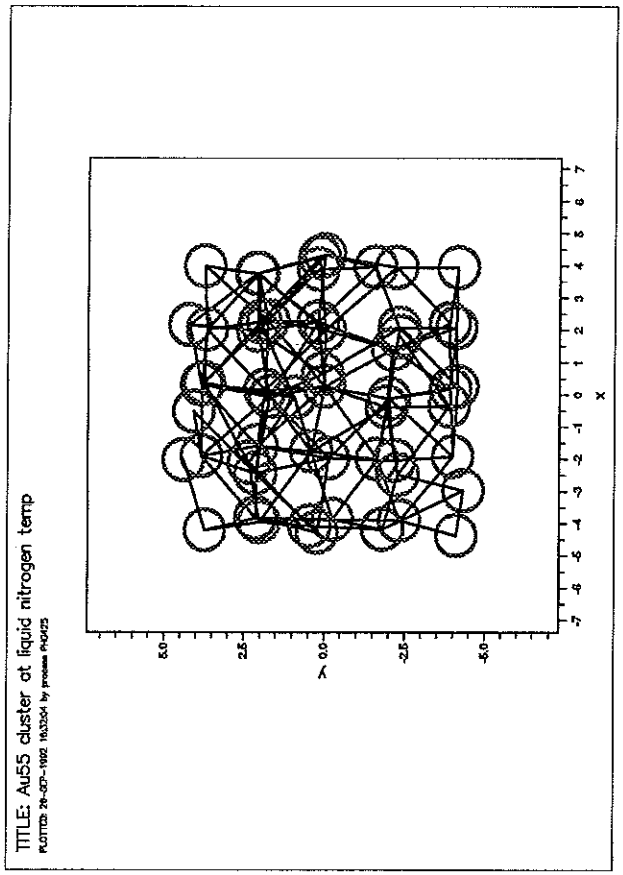

Figure 6.1: Converged RMC configuration, cuboctahedral starting configuration

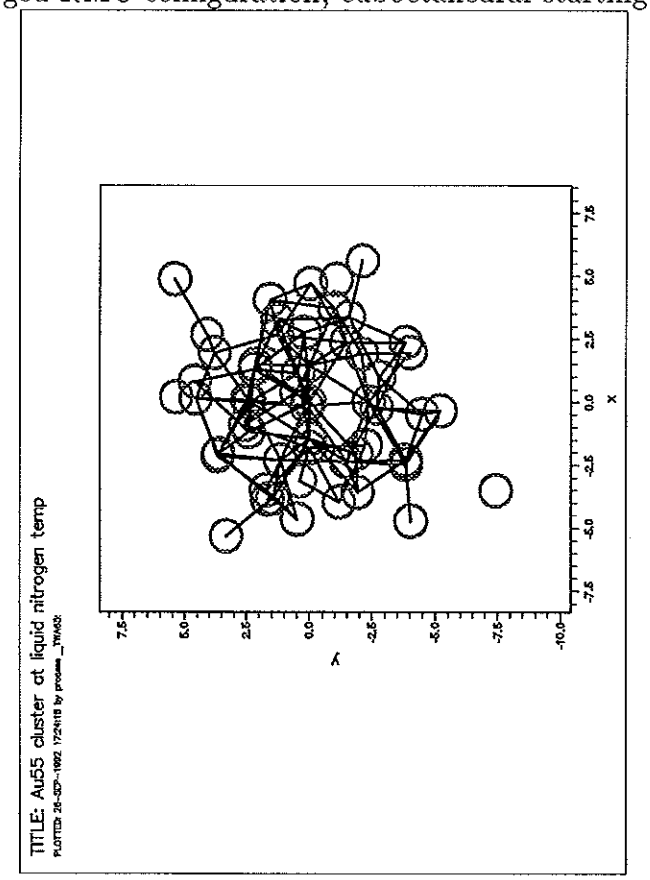

Figure 6.2: Converged RMC configuration, icosahedral starting configuration

Chapter 7

Discussion of Results

7.1 Gold foil

To correct for the contraction in the bond lengths due to the reduced temperature, a linear relationship between temperature and length is assumed, and given that the thermal coefficient of expansion of gold is 14.2 x10^{-6} K^{-1} (from CRC handbook[54]), and using the following formula:

$$\Delta l = l \Delta \theta \alpha_l \tag{7.1}$$

where Δl is the change in bond length, $\Delta \theta$ the change in temperature (approximately 220K) and α_l the coefficient of linear expansion, we obtain a value of 0.009Å as a correction value. Subtracting this from the bond length of gold at room temperature, 2.884Å gives a value of 2.875 - a closer match to the experimental bond length of 2.85Å

Figure 7.1: Variation in total σ^2 for gold foil as a function of temperature

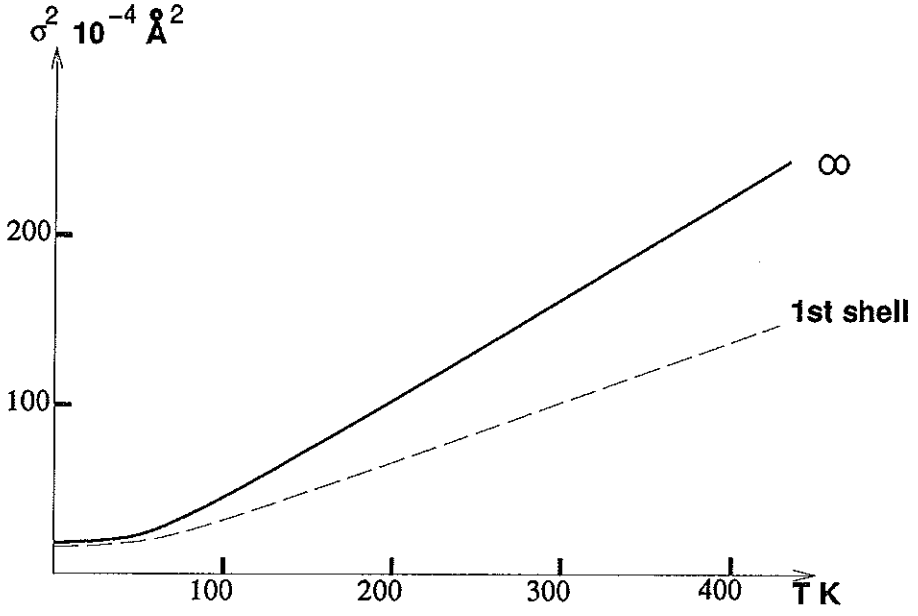

for the first Au-Au distance in the foil at 80K. Taken together, the near neighbour distances for the foil are what would be expected for a close-packed (i.e. Face Centred Cubic) structure.

In what follows, we will be assuming that the clusters have the same zero-point motion as the foil samples. This assumption is based on the fact that at 80K, the samples are well below their Debye temperature (θ_D=162K for gold, and most of the thermally induced order is removed. Figure 7.1 from Gurman[57] illustrates this.

Balerna *et.al* [16] have ignored zero-point motion, and seem to have based their analysis on the assumption that no thermal disorder exists well below the Debye temperature.

The values of AFAC and VPI (A(k) and $e^{-2\lambda/k}$ in the PWA equation 2.4) fall within the limits one would expect for a metallic system[35]. This indicates that the phaseshifts with their respective backscattering factors, F(k), and the Muffin-Tin potentials used to calculate E_0 work sufficiently well here. Alteration of the Muffin-Tin radii is considered here to be an unphysical procedure, and would be avoided even if required for a better fit, as this constitutes varying the the distance over which the potential from each site influences one another. In addition, the Muffin-Tin model is known to work well for a crystalline system, lending itself well to the clusters here.

7.1.1 Palladium Foil

The value of α_l for palladium foil [58] of $11.75 \times 10^{-6} K^{-1}$ yields 0.0071Å as a correction for the foil bond length. Adding this to the experimental value results in 2.74Å for the near neighbour bond length in the foil.

7.2 Gold 11 cluster

As a reasonably small cluster (compared with the larger Au and Pd clusters under study here), the Au_{11} provides a good starting point to gauge the effectiveness of EXAFS on this type of system, i.e. a molecular solid consisting of discrete well defined 'molecules' (which for this sample actually exist in a regular crystal lattice). Having only 11 atoms makes interpretation of X-Ray diffraction results much easier, and

work by Albano[27] has elucidated both the local atomic arrangement and large scale structure of clusters of the general type $Au_{11}L_7X_3$ (where L=PPh_3,SCN ; X=I,Cl)

After correcting the sample for temperature contractions (0.008Å using equation 7.1), a near neighgbour bond distance of 2.67Å at room temperature is obtained; a contraction of 0.21Å from the bulk value (7%), this is considerably larger than the systematic errors and Debye-Waller uncertainty. The contraction is consistent with that expected for a cluster of this size, also being larger than for the larger gold cluster. EXAFS results from this sample clearly shows the evidence of one of the distances corresponding to that of the split peak at 2.88Å (2.89Å corrected for contraction at 80K), found for clusters with an essentially icosahedral geometry[59].

The peaks seen at 4.69Å can be attributed to the second nearest neighbour position of atoms on the surface. An additional Au-Au peak at 5.14Å was observed during the iteration procedure and is shown in the map plot (Figure 4.13), but could not be fitted to 99% significance, and is therefore not shown in the results table. The fact that the surface is comprised of gold atoms in both a square and triangular arrangement could explain why there are two of these peaks in close proximity, but more data regarding the exact distances (via X-ray diffraction results) would be necessary to state definitively the origins of the peaks. As an indication of the high quality of the EXAFS bond lengths quoted, typical bond lengths from a similar Au_{11} cluster ($Au_{11}I_3P_7$ from [60]) are tabulated here:

Distance	X-Ray Diffraction	EXAFS
Au-Au (centre-periphery)	2.69Å(mean)	2.67Å
Au-Au (periphery-periphery)	2.84-3.19Å(mean 2.98Å)	2.89
Au-P	2.21-2.29Å	2.28Å
Au-I	2.60	2.65

Ligand modelling for the EXAFS results compares most favourably with complementary results, and show that P and I are easily differentiated from one another in EXAFS studies. Bond distances are much like those seen in other compounds of the same basic formulation[59, 27].

The values of σ_{80K} for nearest neighbour contributions compare very well with those of the gold foil, indicating virtually no static disorder present. This is a sensible result, as Au_{11} forms a regular crystalline structure in the solid state. Even if the rather large statistical error for the Debye-Waller factor is taken into account, the static disorder for Au_{11} is still appreciably smaller than that for Au_{55}.

7.3 Gold-55 cluster

Adding the 0.009Å correction value gives a near neighbour bond distance of 2.76Å for $Au_{55}(PPh_3)_{12}Cl_6$ ($\pm$0.004Å) which compares favourably with previous results[20] (which had poorer quality data with only one shell fitted), i.e. the average cluster Au–Au bond distance is significantly contracted by around 4% from the bulk Au–Au distance (2.88Å from literature[54]). In work by Marcus [21], the Au-Au distance was found to be 2.80Å ($\pm$0.01Å) for Au_{55} at 8K.

The overall magnitude of the EXAFS signal, and consequently its Fourier transform is diminished significantly from that of the bulk. This is shown in Figure 7.2, and is expected for a system of small particles, i.e. lower average coordination numbers. The figure also highlights the similar nature of the bond length distributions present in the cluster and metallic gold.

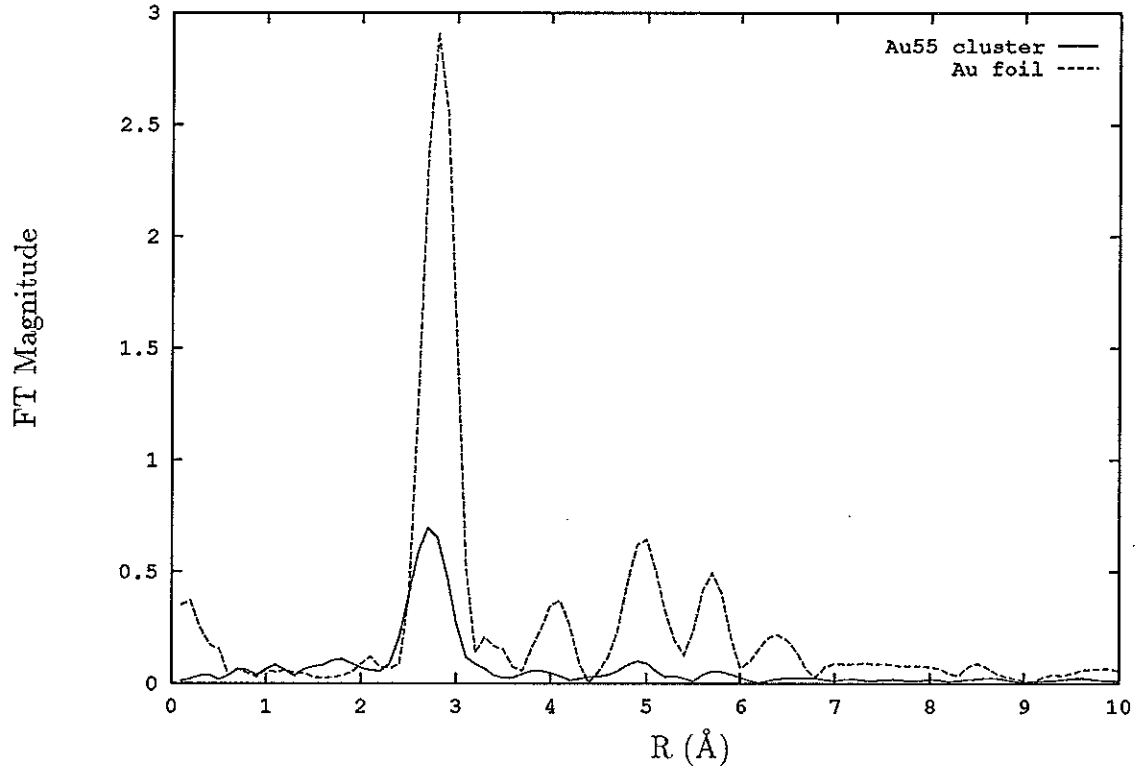

Figure 7.2: Comparison of FT magnitudes for Au_{55} cluster and gold foil

The values for first shell coordination numbers of the cluster agree well with the predicted value of 7.85 for a 55-atom cuboctahedron[17], although within the errors specified the value could also be attributed to an icosahedron. Coordination numbers

however, cannot be measured with great precision in EXAFS and serve only as a guideline in the analysis procedure.

Au-Au distance for the cooled cluster shows contraction from the bulk by up to 6%, somewhat larger than other EXAFS work would seem to indicate. Clearly this work cannot be taken in isolation and work in other areas needs to be taken into account when coming to a conclusion. The Mössbauer results in particular are helpful in identifying the different Au sites, which do seem to be consistent with the model of a sphere of ligands on well defined sites of the surface of the cluster [17]. As no evidence was seen for a split in the main peak in Au_{55}, it is concluded that the polyicosahedral structure proposed by Fackler et.al.[61] does not fit with the experimental results obtained (c.f. Au_{11}) and the cuboctahedral structure is most likely.

If one assumes that the cluster has the same zero-point vibrational energy as the foil, then a value of the mean square displacement of the bonds in the cluster due to static disorder can be found by subtracting σ^2_{80K} for the foil (0.004 Å^2) from σ^2_{80K} for the cluster (0.0095 Å^2) This gives a value of 0.0055 Å^2 for the cluster, which compares extremely well with that of 0.0057 Å^2 found by Marcus[21].

This disorder is probably due to the slightly distorted nature of the cluster. Ligand modelling for this cluster gives results which show that phosphorus and chlorine atoms can be separated in EXAFS analysis. Map plots show that both peaks are highly

correlated, and a *single* minimum exists (Figures 4.20 and 4.21), i.e. a unique location where the optimum values of both parameters lie (showing that the ligand parameters have not been obtained from one of several minima). Although the peaks are distinct, they are sufficiently close to one another (in the periodic table) to necessitate the use of additional evidence in assigning one to phosphorus, and one to chlorine. Fortunately this evidence exists from the Au_{11} cluster work, which has a Au-P bond distance at 2.27Å. The phosphorus peak here is therefore assigned to the 2.3Å peak, and the chlorine to the 2.50Å peak. Values for both peaks fall within the range expected for compounds of this type. In addition, it was found from infra-red studies on the Au_{55} cluster that the Au-Cl bond stretch, ν_{Au-Cl}, was 280cm^{-1} - substantially weaker than that for $Au(PPh_3)Cl$ which was reported as having ν_{Au-Cl}=330cm^{-1} and a Au-Cl bond length of 2.28Å[62]. It is therefore not unreasonable to assume that the Au-Cl bond length will be longer than 2.28Å, as found here. Previous EXAFS work [21] attributed a 2.31Å peak to Cl. It seems likely that this peak was in fact due to a phosphorus contribution to the EXAFS signal.

7.4 Palladium 561 Giant Cluster

Palladium results are less promising with respect to ligand contributions, due perhaps to the larger depth of the metal core in relation to the ligands, which being mainly light atoms, have a much weaker scattering intensity than the metal core. The temperature

corrected near-neighbour distance of 2.75Å is close to that of the bulk, indicating a relatively large cluster.

However definitive conclusions can be made from the bond distances alone, which clearly correspond to the nearest neighbour distances expected from a close packed system, i.e. a_0, $\sqrt{2}a_0$, $\sqrt{3}a_0$, etc. and not an icosahedral distribution, which would possess several intermediate distances. This is to be contrasted to the Russian [?] Pd_{561} sample which was said to be icosahedral. Coordination numbers are unfortunately inconclusive, and Debye-Waller values seem to reflect the bulk nature of the sample, i.e. similar static disorder to bulk palladium.

7.5 Errors

Errors present within EXAFS results are an often overlooked part of the analysis. Here we assume the major contributions to the uncertainty of the results comes from those resulting from the fitting procedure. Other effects such as sample and beam inhomogeneity are considerably less. The major concern amongst EXAFS users is the viability of transferring phaseshifts between calibrant and unknown. This has already been discussed, and given the crystalline nature of the clusters (something which is apparent from the small Debye-Waller Factors and very low statistical errors shown), it is likely that the phaseshifts for the calibrants (foils) model quite closely that of the clusters. Errors quoted are double those given from the iteration process

(see Analysis).

It is noted that errors in coordination numbers (and some Debye-Waller factors) are large, often greater than the value itself. This cannot be avoided, and is one of the less reliable aspects of EXAFS analysis. The causes are partly due to the very small size of the oscillations compared to the height of the edge itself, as well as errors added during the normalisation process. Also, the overlap of the peaks in the Fourier transform of several coordination shells, introducing correlations between different shells will also affect the accuracy of each coordination number.

7.6 Conclusion

It has been demonstrated that not only can EXAFS provide information on the metal-metal bonds present in metallic clusters, but in addition can provide valuable information regarding the ligands bonded to the surface of these clusters. In all of the gold cluster samples studied here, results show a general decrease in the nearest neighbour bond lengths, supported by a stiffening of the bonds shown by the reduced Debye-Waller factors as compared to the bulk samples.

The realisation of the split main peak for the smaller Au_{11} proves that EXAFS is able to resolve these distances, i.e. differences of approximately 5% in the mean bond length.

It is hoped that future work will continue in the characterization of the larger

clusters as they present exciting avenues of research, open to both chemists and physicists. Small Angle X-ray Scattering (SAXS) work would provide a larger insight into the long range structure of the samples, something which could assist in the discussion of whether the palladium cluster has more of a colloidal nature. In the light of the unsuitability of the RMC method, modelling techniques which involve potential calculations (molecular dynamics studies) would perhaps be more appropriate.

Appendix A

Publications

Presentations and publications arising from work within this thesis:

- 'An EXAFS Study of some gold and palladium cluster compounds',

  P.D.Cluskey, R.J.Newport, R.E.Benfield, S.J.Gurman and G.Schmid,

  Zeitschrift fur Physik D,

  Submitted for publication. (Also Presented at the 6th International Symposium on Small Particles and Inorganic Clusters, University of Chicago 1992).

- 'Structural Analysis of Gold Clusters using EXAFS',

  P.D.Cluskey, R.J.Newport, R.E.Benfield, S.J.Gurman and G.Schmid,

  Materials Research Society Spring '92 Conference, presented in San Francisco April 1992.

Bibliography

[1] R.E.Benfield, J.A.Creighton, D.G.Eadon, and G.Schmid. *Z.Phys.D.*, 12:533–536, 1989.

[2] J.Reed, P.Eisenberger, B.K.Teo, and B.M.Kincaid. *J.American Chemical Soc.*, 100:2375–2378, 1978.

[3] J.Reed, P.Eisenberger, B.K.Teo, and B.M.Kincaid. *J.American Chemical Soc.*, 99:5217–5218, 1977.

[4] J.H.Sinfelt. *Science*, 195:641–646, 1977.

[5] G.H.Via, J.H.Sinfelt, and F.W.Lytle. *J.Chemical Physics*, 71(2):690–699, 1979.

[6] G.Schmid. *Structure and Bonding*, (62):51–85, 1985.

[7] K.P.Hall and D.M.P.Mingos. *Progress in Inorganic Chemistry*, 32:237–325, 1984.

[8] M.J.Vargaftik, I.I.Moissev, D.I.Kochubey, and K.I.Zamaraev. *Faraday Discuss. Chem. Soc.*, 92, 1991.

[9] M.J.Vargaftik, I.I.Moissev, D.I .Kochubey, and K.I.Zamaraev. *J.Chem. Soc. Chem. Comm.*, pages 937–939, 1985.

[10] P.A.Lee, P.H.Citrin, P.Eisenberger, and B.M.Kincaid. *Rev.Mod.Phys.*, 53(4):769–806, 1981.

[11] A.Balerna, E.Bernieri, P.Picozzi, A.Reale, S.Santucci, E.Burattini, and S.Mobilio. *Physical Review B*, 31(8):5058–5065, 1985.

[12] A.Balerna and S.Moblilio. *Physical Review B*, 34(4):2293–2298, 1986.

[13] P.A.Montano, J.Zhao, M.Ramanathan, G.K.Shenoy, and W.Schulze. *Physica B*, 158:242–244, 1989.

[14] B.F.G.Johnson, editor. *Transition Metal Clusters.* Wiley, 1980.

[15] S.L.Cook, J.Evans, G.N.Greaves, B.F.G.Johnson, J.Lewis, P.R.Raithby, P.B.Wells, and P.Worthington. *J.Chem. Soc. Chem. Comm.*, (14):777–779, 1983.

[16] A.Balerna, E.Bernieri, P.Picozzi, A.Reale, S.Santucci, E.Burattini, and S.Mobilio. *Surface Science*, 156:206–213, 1985.

[17] G.Schmid. *Polyhedron*, 7:2321–2327, 1988.

[18] H.H.A.Smit, R.C.Thiel, L.J. de Jongh, G.Schmid, and N.Klein. *Solid-State Communications*, 9(65):915–920, 1988.

[19] H.H.A.Smit, P.R.Nugteren, R.C.Thiel, and L.J. de Jongh. *Physica B*, 153:33–52, 1988.

[20] M.C.Fairbanks, R.E.Benfield, R.J.Newport, and G.Schmid. *Solid-State Communications*, 73(6):431–436, 1990.

[21] M.A.Marcus, M.P.Andrews, and J.Zegenhagen. *Physical Review B*, 42(6):3312–3316, 1990.

[22] H.Feld, A.Leute, D.Rading, A.Benninghoven, and G.Schmid. *J.American Chemical Soc.*, 112:8166–8167, 1990.

[23] R.E.Benfield. *J.Organometallic Chemistry*, 372:163–169, 1989.

[24] M.P.J. van Staveren, H.B.Brom, and L.J. de Johgh. *Solid-State Communications*, 60(4):319–322, 1986.

[25] U.Simon, G.schmid, and G.Schon. In *MRS Spring '92 conference*, 1992.

[26] M.McPartlin, R.Mason, and L.Malatesta. *J.Chem. Soc. Chem. Comm.*, page 334, 1969.

[27] V.G.Albano, P.L.Bellon, M.Manassero, and M.Sansoni. *J.Chem. Soc. Chem. Comm.*, pages 1210–1211, 1970.

[28] F.Cariati and L.Naldini. *Inorganica Chimica Acta*, 5(2):172–174, 1971.

[29] A.L.Mackay. *Acta Cryst.*, 15:916–918, 1962.

[30] R.B.King. *Prog.Inorg.Chemistry*, 15:452–454, 1972.

[31] H.A.Wierenga, L.Soethout, J.W.Gerritsen, B.E.C. van de Leemput, H. van Kempen, and G.Schmid. *Advanced Materials*, 2(10), 1990.

[32] N.W.Ashcroft and N.D.Mermin. *Solid State Physics.* Holt-Saunders, 1976.

[33] P.A.Lee and J.B.Pendry. *Physical Review B*, 11(8):2795–2851, 1975.

[34] S.J.Gurman, N.Binstead, and I.Ross. *J.Physics: Solid State Physics*, 17:143, 1984.

[35] S.J.Gurman. *Synchrotron Radiation and Biophysics.* Ellis-Horwood, 1990.

[36] H.Peterson. *Z. Phys.*, 76:768, 1932.

[37] M.Sawada. *Rep. Sci. Workshop Osaka Univ.*, 7:1, 1959.

[38] V.V.Schmidt. *Bull. Acad. Sci. USSR, Phys Ser.*, 25, 1961.

[39] D.E.Sayers, E.A.Stern, and F.W.Lytle. *Physical Review Letters*, 27(18), 1971.

[40] E.A.Stern. *Physical Review B*, 10(8):3027–3037, 1974.

[41] C.A.Ashley and S.Doniach. *Physical Review B*, 11:1279, 1975.

[42] S.J.Gurman. *J.Physics: Solid State Physics*, 21:3699–3717, 1988.

[43] P.H.Citrin, P.Eisenberger, and B.M.Kincaid. *Physical Review Letters*, 36(22):1346–1349, 1976.

[44] A.Murari and A.R.Chetal. *Phys.stat.sol.*, 170:391–394, 1992.

[45] D.T.Bowron. private communication. 1992.

[46] B.K.Teo. *EXAFS: Basic Principles and Data Analysis.* Springer-Verlag Berlin Heidelberg New York Tokyo, 1986.

[47] D.C.Koningsberger and R.Prins. *X-Ray Absorption: Principles, Applications, Techniques of EXAFS, SEXAFS and XANES.* Wiley, 1988.

[48] Excurv90 user manual. Technical report, Daresbury SRS Laboratory, Warrington, U.K., 1989.

[49] Joyner, Martin, and Meeham. *J.Physics.C*, 20:4005, 1987.

[50] A.M.Edwards. *The Structure of Amorphous Semiconductor:Metal Thin-Films.* PhD thesis, University of Kent at Canterbury, November 1989.

[51] S.M.Heald. *X-Ray Absorption: Principles, Applications,Techniques of EXAFS, SEXAFS and XANES*, chapter 3. Wiley, 1988.

[52] J.Jaklevic, J.A.Kirby, M.P.Klein, A.S.Robertson, G.S.Brown, and P.Eisenberger. *Solid-State Communications*, 23:679–682, 1977.

[53] S.S.Hasnain, P.D.Quinn, G.P.Diakun, E.M.Wardell, and C.D.Garner. *J.Phys.E: Sci.Instruments*, 17:40–43, 1984.

[54] *CRC Handbook of Chemistry and Physics.* CRC Press, 1981. hardbound edition, section D189.

[55] K.F.G.Brackenbury, L.Jones, I.Nel, K.R.Koch, and J.M.Wyrley-Birch. *Polyhedron*, 6(1):71–78, 1987.

[56] S.J.Gurman and R.L.McGreevy. *J.Physics: Condensed Matter*, 1990. submitted for publication.

[57] S.J.Gurman. private communication, 1992.

[58] J.D.Donohue. *The Structure of the Elements.* Wiley, New York, 1974.

[59] P.L.Bellon, F.Cariati, M.Manassero, L.Naldini, and M.Sansoni. *J.Chem. Soc. Chem. Comm.*, pages 1423–24, 1971.

[60] P.Bellon, M.Manassero, and M.Sansoni. *J.Chem.Soc.Dalton*, pages 1481–1487, 1972.

[61] J.P.Fackler Jr., C.J.McNeal, R.E.P.Winpenny, and L.H.Pignolet. *J.American Chemical Soc.*, 111:6434–6435, 1989.

[62] P.D.Cluskey, R.J.Newport, R.E.Benfield, S.J.Gurman, and G.Schmid. *Zeitschrift fur Physik D*, 1992. Submitted for publication.